3-2022

Magnetic Flux Channel Antenna Design in Conformal Applications

William J. Tremblay

MAGNETIC FLUX CHANNEL ANTENNA DESIGN IN CONFORMAL APPLICATIONS

THESIS

William J. Tremblay, Captain, USAF

AFIT-ENG-MS-22-M-069

DEPARTMENT OF THE AIR FORCE
AIR UNIVERSITY

AIR FORCE INSTITUTE OF TECHNOLOGY

Wright-Patterson Air Force Base, Ohio

AFIT-ENG-MS-22-M-069

MAGNETIC FLUX CHANNEL ANTENNA DESIGN IN CONFORMAL APPLICATIONS

THESIS

Presented to the Faculty

Department of Electrical and Computer Engineering

Graduate School of Engineering and Management

Air Force Institute of Technology

Air University

Air Education and Training Command

in Partial Fulfillment of the Requirements for the

Degree of Master of Science in Electrical Engineering

William J. Tremblay, B.S.E.E.

Captain, USAF

March 24, 2022

AFIT-ENG-MS-22-M-069

MAGNETIC FLUX CHANNEL ANTENNA DESIGN IN CONFORMAL APPLICATIONS

THESIS

William J. Tremblay, B.S.E.E.
Captain, USAF

Committee Membership:

Michael D. Seal, Ph.D.
Chair

Andrew J. Terzuoli,, Ph.D.
Member

Spencer R. Sellers,, Ph.D.
Member

Abstract

Magnetic Flux Channels (MFC) and Magneto-Dielectric Wire Antennas (MDWA) are effective, and in some cases, superior alternatives to traditional metallic antennas, particularly in conformal and electrically small applications at the cost of fabrication and feed complexity. The frequency dispersive nature of magnetic material constituent parameters imposes operating frequency constraints on the antenna design process, which were not fully developed in prior art. This research quantifies the key differences between the operating regions of magneto-dielectric materials for antenna applications and demonstrates the effectiveness of numerical method augmented modal analysis in the design process, regardless of operating region. Modeling challenges associated with MDWAs are addressed leading to novel full wave modeling results for antennas designed in accordance with early MDWA design law. The results clarify the limitations of certain prior art in the recommended design process, and provide needed support for later-art material selection and design recommendations.

Table of Contents

List of Figures

List of Tables

MAGNETIC FLUX CHANNEL ANTENNA DESIGN IN CONFORMAL APPLICATIONS

I. Introduction

1.1 Problem Background

Antenna design processes for purely electromagetic performance are well established. However, most applications include other physical design requirements which dominate the design trade space. For example an antenna that protrudes from the body of an aircraft several feet imposes significant drag, so blade antennas are employed that trade off some of the electromagnetic capability of that antenna in order to reduce the drag the antenna puts on the aircraft. However, there are limits to how conformal an antenna can be made ans still meet frequency and gain requirements. This limitation stems primarily from the impact of electric image currents over a metallic ground plane, in vehicular applications. One of the few methods of directly addressing the image current induced limitations are Magneto-Dielectric Wire Antennas (MDWA)s and Magnetic Flux Channels (MFC)s.

MDWA were shown to be a dual to traditional electric antennas by Sebastian, with the additional advantages in conformal applications near a ground plane [1]. These advantages drove the prior art research effort, which sought to develop efficient design laws for this antenna type. However, after 2020 publication on this type dies off, with only a single commercially successful design [2]. The research chain left some key items on the table. This research sought to complete and extend some elements of the original work.

1.2 Research Objectives

This thesis extends and completes some elements of the body of work investigating the use of magneto-dielectrics as antennas for conformal, electrically small applications under previously unpublished conditions. The overall objective is to advance the state of the design guidance discourse to drive future material and application considerations. Specific contributions include, the use of additional analytic alternatives to estimate cutoff frequencies, the application of 2D Finite Difference Time-Domain (FDTD) simulations to dertermine modal cutoff frequencies, the investigation of full-wave simulations to model several MDWA configurations and feed structures, further investigation into the impact of several design simplifications in the original work, and a more complete analysis of three material driven distinct operating regions available for MDWA concepts.

1.3 Document Overview

This thesis is presented in seven chapters. Chapter II presents relevant background obtained from literature and sets a baseline for the current state of the art of MDWAs and MFCs. Chapter III identifies and extends the recommended analytic estimation methods for cutoff frequencies of certain designs. Chapter IV presents full-wave simulations of MDWAs and MFCs. Chapter V demonstrates the utility of employing 2D FDTD simulations to predict the cutoff frequencies of antenna cross sections. Chapter VI explores full-wave simulations of feed structures to identify limitations. Chapter VII incorporates the claims made from Chapters III, IV, V, and VI into a design method and then extends those claims to different antenna configurations and operating regimes as well as highlighting several oversimplifications in prior art. Chapter VIII provides a summary and conclusion based on the results as well as proposed future research in this area.

II. Background and Literature Review

This chapter presents information critical to a comprehensive understanding of Magneto-Dielectric Wire Antennas (MDWA) and their design. It begins with an explanation of how magneto-dielectric materials influence the solutions of Maxwell's Equations and leads to a description of how it applies to MDWA design criteria. A brief history is of prior art given, explaining why the MDWA concept has not been explored until recently using high loss materials. Then the value of MDWAs in conformal applications compared to their electric antenna counterparts is elucidated. A variety of prior art antenna configurations are presented and reviewed. Finally, a brief modal analysis development is presented, setting a foundation for this work's extension of MDWA design methodology.

2.1 Magneto-Dielectric Antenna History

Lossy magneto-dielectrics are not new in Radio Frequency (RF) engineering. In particular, engineers including Giri were investigating electrically small loop antennas loaded with low but meaningful loss ferrites as early as 1973 [3]. Most of the work prior to the 21st century was focused on nearly lossless materials and the majority of concepts only used magneto-dielectrics to load metallic antennas to reduce their size. It wasn't until the late 2000s when the concept of using lossy magneto-dielectrics as the radiating structure instead of simply loading metallic antennas became a research focus for a few companies and academic institutions [1, 4, 5]. Arizona State University (ASU) and *JEM Engineering* are significant contributors to the development and deployment of magneto-dielectric wire antennas.

The first major piece considered in this work is Tom Sebastian's dissertation completed in 2013 at ASU [1]. This work was the keystone piece which provided the

theoretical contribution which enabled the development of magneto-dielectric wire antennas. Specifically, it provided the correction to the efficiency equation utilization from DeVore [1]. The work and concept was significantly extended by Tara Yousefi in her dissertation which was completed in 2017 [5] also at ASU. In her dissertation, Yousefi addressed several unexplored areas from Sebastian's dissertation in particular shifting from high imaginary permeability to lower imaginary permeability. In particular, Yousefi introduced the concept Magnetic Flux Channels (MFC) and addressed the benefits of a vertical laminate substrate of a magneto-dielectric material sputtered on a film, as compared to a monolithic material.

In addition to the work of Yousefi and Sebastian in their dissertations, there were several Small Business Innovation Research (SIBR) contracts let on this topic with which ASU was involved [2, 4, 6, 7]. These SIBR contracts provided reports for the government between 2014 and 2020 and the research results contributed to the commercialized products of *JEM Engineering*, as the SBIR program is intended to do. This work seeks to fill in a limited selection of information gaps found in the published literature and the final reports. These gaps include using analytic alternatives to find modal cutoff frequencies, applying 2D Finite Difference Time-Domain (FDTD) methods to refine modal cutoff estimates and study feed type implications, and addressing the sources of full-wave simulation challenges in modeling MDWA antenna designs. Given these aims a focused exposition of Maxwell's Equations is in order to highlight the less common radiation modes employed by MDWAs and MFCs.

2.2 Maxwell's Equations for Magneto-Dielectrics

Maxwell's Equations as refined by Oliver Heaviside introduced a fictitious magnetic current and magnetic charge density to maintain symmetry. As such Maxwell's

Equations are written as follows in differential form:

$$\nabla \times H = \frac{\partial D}{\partial t} + J_e \tag{1}$$

$$\nabla \times E = \frac{\partial B}{\partial t} + J_m \tag{2}$$

$$\nabla \cdot D = \rho_e \tag{3}$$

$$\nabla \cdot B = \rho_m \tag{4}$$

Maxwell's Equations are not well posed without material properties introduced through the constitutive relations, $D = \epsilon_o \epsilon_r E$ and $B = \mu_o \mu_r H$, with the magnetic flux density, B being the most critical to this work. Using the constitutive relations Maxwell's Curl Equations:[1]

$$\nabla \times H = \frac{\partial D}{\partial t} + J_e = \epsilon_o \frac{\partial E}{\partial t} + \epsilon_o(\epsilon_r - 1)\frac{\partial E}{\partial t} + J_e = \epsilon_o \frac{\partial E}{\partial t} + \frac{\partial P_e}{\partial t} + J_e \tag{5}$$

$$\nabla \times E = \frac{\partial B}{\partial t} + J_m = \mu_o \frac{\partial H}{\partial t} + \mu_o(\mu_r - 1)\frac{\partial H}{\partial t} + J_m = \mu_o \frac{\partial H}{\partial t} + \frac{\partial P_m}{\partial t} + J_m \tag{6}$$

For metallic antennas, including dielectrically loaded antennas, where $\epsilon_r \gg \mu_r$, the electric current, J_e, and electric polarization current density, $\frac{\partial P_e}{\partial t}$, are the source of radiation. Conversely, for magneto-dielectric antennas, $\mu_r \gg \epsilon_r$, there is no physical magnetic current, J_m, so the only source of radiation is the magnetic polarization current density, $\frac{\partial P_m}{\partial t}$, where $\frac{\partial P_m}{\partial t} = \mu_o(\mu_r - 1)\frac{\partial H}{\partial t}$ [1]. Therefore, the complex permeability is the key parameter effecting the potential radiation efficiency of a magneto-dielectric antenna.

2.3 Magnetic Antenna Radiation Efficiency

Efficient radiation can be achieved by magnetic dipoles and permeable ferrite dipole antennas. Both were investigated and used throughout the 20th century, based on key research by Rumsey then by DeVore [8]. Both made the assumption that low loss materials, $\mu' >> \mu''$, were the only viable option because losses were expected to decrease the radiation efficiency, based on the model presented in Equation 7 [8]. In Equation 7, the radiation efficiency of an electrically small ferrite dipole rod, where ρ is the radius of the dipole, l is the length of the dipole and k is the wavenumber is shown as derived by DeVore in 1977 [8].

$$Eff_{ferriterod} = \frac{1}{1 + \frac{6}{(kl)^3\left(\frac{\rho}{l}\right)^2}\frac{\mu''}{\mu'^2}} \tag{7}$$

The radiation efficiency derived by Rumsey and DeVore imposed the assumption of low loss materials and ignored permittivity, inaccurately implying the conclusion that radiation efficiency can only be improved by increasing the real permeability (μ') or by decreasing the imaginary permeability (μ''). At the time of this development permeable materials were not well established and further investigation had to wait for materials spanning the spectrum of μ'' for different loss values [8]. Tom Sebastian reattacked the efficiency equation in more general form in his dissertation developing a circuit model for a dielectric dipole with a uniform current distribution. He invoked duality to establish that the radiation efficiency of a purely magnetic dipole may be expressed as shown in Equation 8 [1].

$$Eff_{magonly} = \frac{1}{1 + \frac{\mu''}{|\mu_r - 1|^2}\frac{6}{\left(\frac{\rho}{l}\right)^2(kl)^3}} \tag{8}$$

Upon inspection of Equation 8 it becomes clear that high radiation efficiency can

be achieved using either high loss $\mu'' >> \mu'$ or low loss $\mu'' << \mu'$. This validates Rumsey and DeVore's early development, as a subset of cases, while suggesting that a broader field of materials can be used for magnetic radiation elements based on high magnetic loss values.

While potential dipole radiation efficiency is a limited tool for antenna design it provides a useful benchmark for material selection. A contour plot of the efficiency for a fixed frequency and size but varying μ'' and μ' values is shown in Figure 1. It should be noted that there are three distinct regions where high radiation efficiency can be achieved. Region 3 is the low loss region that Rumsey and DeVore identified. Region 2 is a difficult design region where both μ' and μ'' are large, and finally region 1 is the high loss region and the focus of Sebastian's research [1]. The green lines in Figure 1 indicate the approximate transition point between these operating regions.

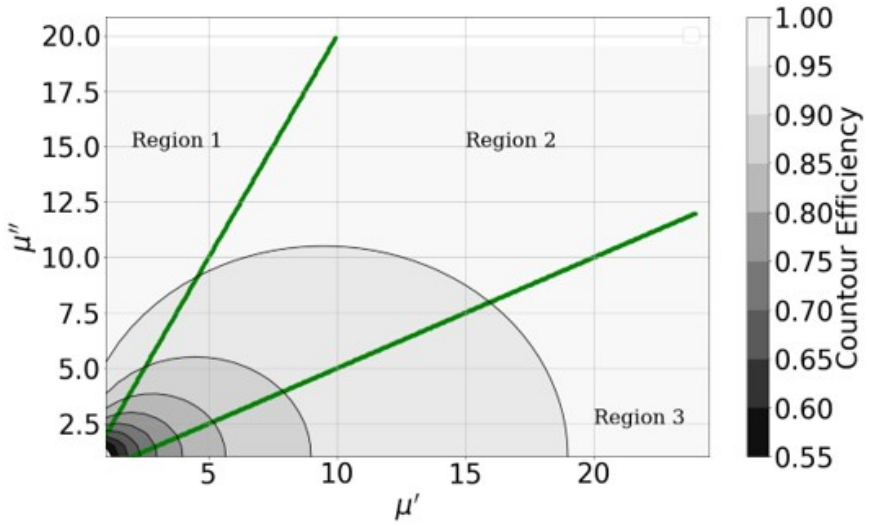

Figure 1: Example radiation efficiency contour plot versus μ' and μ''. Regions 1, 2, and 3 all provide greater that 90% radiation efficiency. Region 3 includes low loss material $\mu' > 20$, Region 2 is defined by both μ' and μ'' having large values, and Region 1 occurs where high loss, $\mu'' > 10$ and low real $\mu' < 5$ values of permeability are exhibited. The contours shown are for a fixed size dipole.

2.3.1 Electrically Small Dipole Radiation Efficiency

The validity of achieving high efficiency from high loss materials was established using purely magnetic material and a uniform current distribution along a dipole, in Section 2.3. However, looking towards more realistic material models, purely magnetic material cannot be assumed. Typically, permittivity values will be found roughly the same magnitude as permeability at frequencies for which significant permeability is exhibited. The more general form of the dipole efficiency, Equation 8, includes the permittivity. Additionally, the assumption of a triangular current distribution introduces new variables into the model. The Area Factor (AF) in Equation 9 is based on the radius of the dipole ρ and the skin depth δ the formula for which is shown in Equation 10 [1]. The first three additional terms expand the radiation efficiency equation, attempting to improve the radiation efficiency calculation at the expense of simplistic design laws.

$$AF = \frac{2\rho\delta - \delta^2}{\rho^2} \tag{9}$$

$$\delta = \frac{1}{Im\left(k_o\sqrt{\mu_r\epsilon_r}\right)} \tag{10}$$

Next the Field Shape Factor (FSF), Equation 11 is introduced and it again uses the radius of the dipole and δ defined in Equation 10. The AF, δ, and FSF are all incorporated into Equation 12, to express the radiation efficiency of an electrically small dipole with a triangular current distribution [1]. It should be noted that the complete complex permittivity and permeability terms are carried into the AF and FSF expressions although they are not explicitly shown in Equations 11 and 12.

$$FSF = \frac{1}{\left(\frac{\delta}{\rho}\right)^2}\left[1 - \frac{8}{3}\left(1 - \frac{\delta}{\rho}\right) + 2\left(1 - \frac{\delta}{\rho}\right)^2 - \frac{1}{3}\left(1 - \frac{\delta}{\rho}\right)^4\right] \tag{11}$$

$$Eff_{triangle} = \frac{1}{1 + \frac{\mu''}{|\mu_r - 1|^2}\frac{8}{AF\left(\frac{\rho}{l}\right)^2(kl)^3} + \frac{\epsilon''}{(kl)}FSF} \tag{12}$$

The radiation efficiency for a triangular current distribution case was calculated for multiple permeabilities, while varying the electrical size and the results are shown in Figure 2. With all other parameters held constant, higher radiation efficiencies are achieved for higher loss permeable materials. Figure 2 must then be interpreted with care, because as the length of the dipole increases the radiation efficiency will increase as well, and may violate the electrically small limit. In addition, the real to imaginary ratio of permeability are 1:1, and therefore this is a region 2 case, which earlier authors did not explore [1, 5]. Further, this derivation is done for electrically small antennas with a triangular current distribution, and when the dipole length becomes too great not all of the antenna will contribute to the radiation. Therefore such an antenna will exhibit a maximum radiation efficiency below 0 dB.

To ensure the entire antenna length contributes to radiation as the antenna size is increased a uniform current distribution must be achieved, typically by driving multiple feed loops. The radiation efficiency equation, derived by Sebastian, for a uniform current distribution for magneto-dielectric materials is shown in Equation 13. All of the variables are the same as those for the triangular current distribution, Equation 12, but the weighting coefficients are modified to reflect the uniform current distribution [9]. In particular, the factor of 8 becomes a 6 in front of the AF and a factor of $\frac{3}{4}$ scales the FSF. This benefits the radiation efficiency by driving the non-unity terms in the denominator closer to zero, a condition which leads to maximum efficiency.

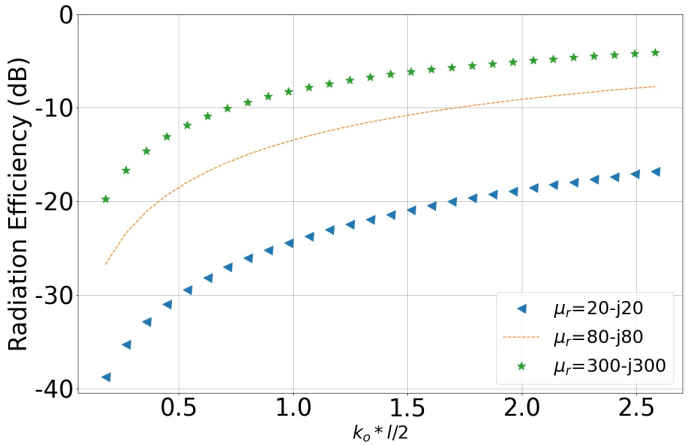

Figure 2: Radiation Efficiency of an electrically small dipole with a triangular current distribution for $\epsilon_r = 14 - j0.7$ Each permeability exhibits different radiation efficiency, and it can be observed that higher permeability leads to increased radiation efficiency.

$$Eff_{uniform} = \frac{1}{1 + \frac{\mu''}{|\mu_r - 1|^2} \frac{6}{AF\left(\frac{\rho}{l}\right)^2 (kl)^3} + \frac{3}{4} \frac{\epsilon''}{(kl)} FSF} \tag{13}$$

Results from Equation 13 are shown in Figure 3 with a single permittivity value tested against several different permeabilities to demonstrate the impact that large permeability values have on radiation efficiency. In this case a moderate real permittivity, but high loss, $\epsilon_r = 10 - j100$, was chosen to represent more realistic magneto-dielectric materials with non free space permittivity. The ferrites Sebastian used in practice exhibited much lower permittivity values, concurrent with their lower real permeabilities [1]. While all of the radiation efficiency curves in Figure 3 follow the same form those with the larger permeabilities demonstrate greater radiation efficiencies compared to those with lower permeabilities.

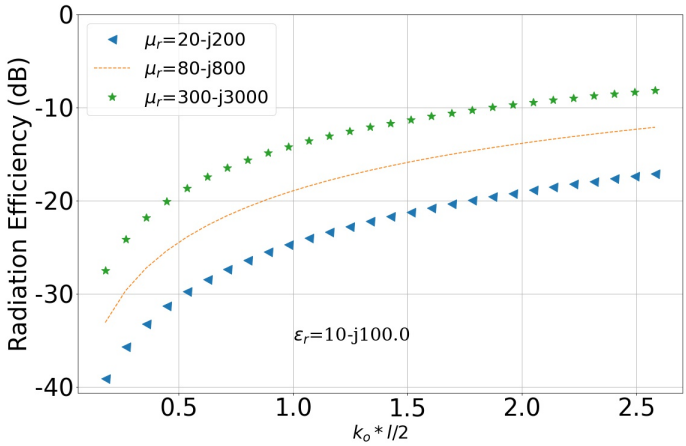

Figure 3: Radiation Efficiency versus electrical length of a magnetic dipole. Three different permeabilities are shown for a moderately high permittivity ($\epsilon_r = 10 - j100$). Higher permeability dipoles exhibit higher radiation efficiency compared to less permeable materials, following the trend predicted by Sebastian.

Based on the results shown in Figure 3, this section demonstrated that electrically small dipole antennas radiate efficiency for both low loss permeable materials and highly lossy permeable materials. Sebastian used this observation to establish the high loss case for MDWAs, essentially emulating a Perfect Magnetic Conductor (PMC) condition by forcing the fields to the exterior of the material [1]. From the derived efficiency equation, Equation 13, it is evident that increasing the loss term of permeability results in high radiation efficiency, as was demonstrated [1]. However, a dipole isn't the ideal form for a magnetic antenna due to its radiation pattern which is not radially symmetric. For a magnetic radiator, a loop antenna produces a radiation pattern more similar to an electric vertical dipole. This radiation pattern is more useful in conformal applications where the objective is to replace a vertical electric dipole, and builds off of the development in this section.

2.3.2 Electrically Small Loop Antenna

The magneto-dielectric dipole antenna previously described, has an undesirable radiation pattern, as it generates a figure-8 pattern along its broadside or in the azimuth plane if installed on a horizontal ground plane. To create an omnidirectional antenna in the azimuth plane a magneto-dielectric loop antenna is the next most simple option. Based on a development similar to that in Tom Sebastian's Dissertation the radiation efficiency of both purely magnetic materials and magneto-dielectrics are expressed in Equations 14 and 15, using a uniform current distribution, where a is the radius of the loop [5].

$$Eff_{magonly} = \frac{1}{1 + \frac{\mu''}{|\mu_r - 1|^2} \frac{12/\pi}{\left(\frac{\rho}{a}\right)^2 (ka)^5}} \tag{14}$$

$$Eff_{uniform} = \frac{1}{1 + \frac{\mu''}{|\mu_r - 1|^2} \frac{12/\pi}{AF\left(\frac{\rho}{a}\right)^2 (ka)^5} + \frac{3}{2\pi} \frac{\epsilon''}{(ka)^3} FSF} \tag{15}$$

Radiation efficiency examples for electrically small loop antennas are plotted for different material properties in Figure 4. It should be noted that the frequency varies along the x-axis, which changes the electrical length of the antenna across the electrically small antenna regime even for constant permeability values.

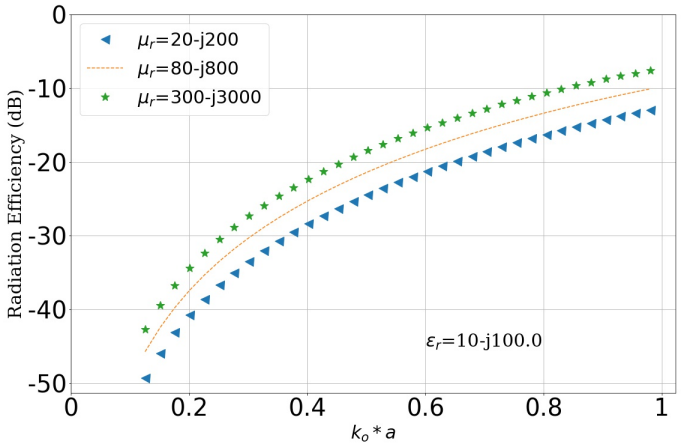

Figure 4: Radiation Efficiency versus electrical length of a magnetic loop antenna. Three different permeabilities are shown with a moderately high permittivity ($\epsilon_r = 10 - j100$). Higher permeability loops demonstrate higher radiation efficiency compared to less permeable materials, which is the same result oberved in the dipole configuration. The primary difference is the radiation pattern.

In Figure 4 it is clear that while each case of permeabilities exhibit the same general behavior with frequency, the material with the largest permeability generates a higher radiation efficiency than its less permeable counterparts. This is the same conclusion that was reached for magnetic dipole antennas [1]. Critically, this result validates that high loss permeable materials can be used as radiators in either dipole or loop configurations, with loop configurations are more generally comparable to electric dipoles due to their radiation pattern.

This section demonstrated radiation efficiency equations for arbitrary permeability and permittivity values highlighting the validity of using high loss magneto-dielectrics as radiators. The primacy of material parameters on performance is established, in as much as both electrically small dipole and loop radiator configurations generated similar radiation efficiency. The next section expounds upon the material properties required of good material candidates.

2.4 Magnetic Material Properties Selection Guidance

With the concept of MDWAs established, attention was focused on realizable materials and their properties [1]. Magnetic materials have been investigated extensively and can be broken into several relevant categories including; diamagnetic, paramagnetic, ferromagnetic, antiferromagnetic, and ferrimagnetic. In general, magnetic material can either aid or oppose an applied magnetic field resulting in different values of the magnetic susceptibility, χ_m. Diagmagnetic, paramagnetic, and antiferromagnetic materials all produce a small χ_m such that the relative permeability remains $\mu_r \approx 1$ for engineering applications, removing them from consideration [10]. This leaves to ferromagnetic and ferrimagnetic magnetic materials as viable material types for high loss antenna applications in this paper.

Ferromagnetic materials have a net zero magnetization vector in the absence of an applied magnetic field [10]. Individual atoms have strong magnetic moments and tend to align near several neighbors forming domains. However, each domain may have a random orientation relative to others resulting in a net zero magnetization vector [10]. Once a magnetic field is applied to the material all of the strong domains align, resulting in large magnetic susceptibility and a large relative permeability. Due to their large permeability values ferromagnetic materials are commonly used in transformers, induction cores, and coatings for magnetic recording tapes [10].

Ferrimagnetic materials have large magnetic moments, but adjacent moments are not uniform without an applied magnetic field. Applying a magnetic field results in large magnetic susceptibilities and in turn permeability. Ferrimagnetic materials have large permeabilities, but not as large as ferromagnetic materials making them good candidates, but ferromagnetic materials have more potential [10]. Typical materials in the ferrimagnetic classification are ferrites such as NiZn. Ferrimagnetic materials have traditional roles in microwave circuit design such as circulators, isolators, gyrators,

and Electromagnetic Interference (EMI) chokes [10].

In both cases, the permeability will display strong frequency dependence. The frequency dependence of a materials permittivity and permeability are analytic functions that satisfy the requirements of causality, linearity, and energy conservation through Kramers-Krönig Relations. These relations were exploited by Sebastian to derive a new material performance metric called Hesitivity, which will be investigated later in this section [1]. Common models for constituent parameters include, the Debye and Lorentz functions, both of which obey the Kramers-Krönig Relations. The Debye and Lorentz functions were originally established as oscillator models for permittivity, but with Heavisides' addition to Maxwell's Equations the Debye and Lorentz functions apply equally to permeability through duality. The Debye and Lorentz equations for magnetic susceptibility are shown in Equations 16 and 17 [1]. In Figures 5 and 6 the real and imaginary parts of the magnetic susceptibility of a notional material are plotted against a normalized frequency f_o of 1.6 GHz, ω_o of $f_o 2\pi$, and a χ_{dc} of 75. In Equations 16 and 17 χ_{dc} is the magnetic susceptibility at DC, ω_o is the radian relaxation frequency, and α is the damping factor for the Lorentz function.

$$\chi_{Deb} = \frac{\chi_{dc}}{1 + j\frac{\omega}{\omega_o}} \tag{16}$$

$$\chi_{Lor} = \frac{\chi_{dc}}{1 + j\frac{\omega}{\omega_o}\alpha - \left(\frac{\omega}{\omega_o}\right)^2} \tag{17}$$

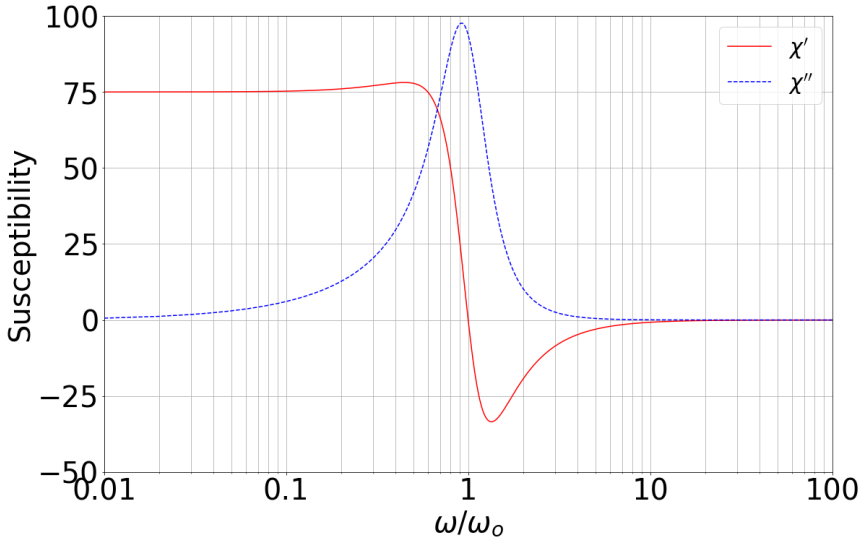

Figure 5: A Single Lorentz susceptibility example. The initial susceptibility is 75 with a resonant frequency of 1.6 GHz. There is clear resonance at the resonant frequency with the imaginary susceptibility peaking higher than the real susceptibility.

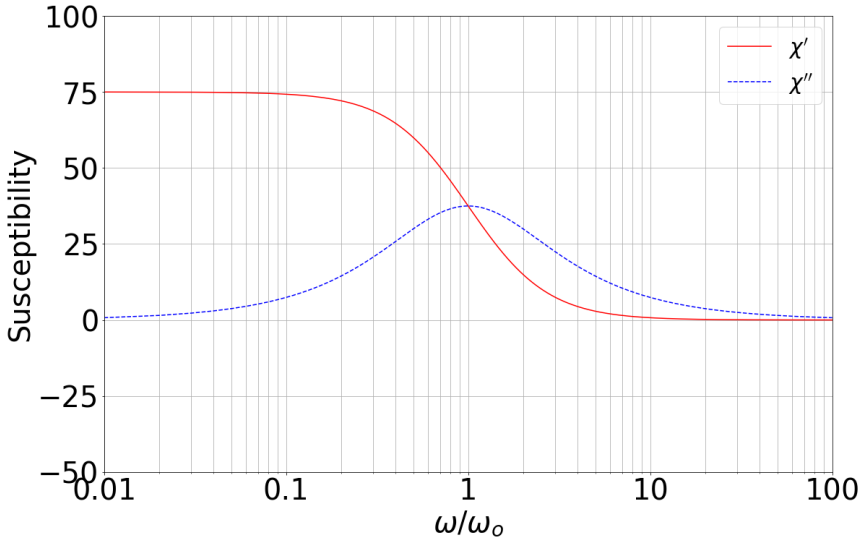

Figure 6: A Single Debye susceptibility example. The initial susceptibility is 75 with a center frequency of 1.6 GHz. Just to the left of resonance where the real susceptibility is large and losses start increasing presents ideal Region 3 behaviors. The gentler transition region around resonance stabilizes the material behavior as resonance is approached.

Lorentz materials can exhibit Region 1, high loss region, operation at resonance whereas Debye materials have to operate to the right of resonance in order to achieve

Region 1 operation. While the most fundamental, susceptibility is not the typical constituent parameter considered by electrical engineers, but rather permeability. Most commercial magnetic materials provide Direct Current (DC) permeability data, and the Debye and Lorentz equations can be extended to permeability through the Equations 18 and 19 [11].

$$\mu_{Deb} = \mu_o \left(1 + \frac{\mu_{dc} - 1}{1 + j\frac{\omega}{\omega_o}} \right) \tag{18}$$

$$\mu_{Lor} = \mu_o \left(1 + \frac{\mu_{dc} - 1}{1 + j\frac{\omega}{\omega_o}\alpha - \left(\frac{\omega}{\omega_o}\right)^2} \right) \tag{19}$$

For the above equations μ_{dc} is the initial permeability of the material. μ_{dc} is related to χ_{dc} by $\mu_{dc} = \frac{\chi_{dc}}{\mu_o} + 1$. For the previous example using the initial susceptibility the real and imaginary parts of the resulting permeability are plotted in Figures 7 and 8. The same general form as the susceptibility plots is retained in the permeability plots.

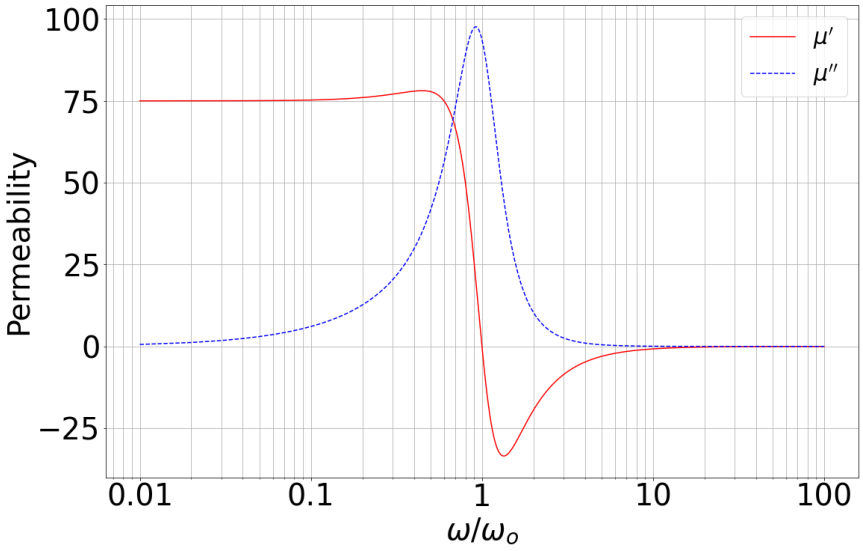

Figure 7: Single Lorentz permeability example. Initial susceptibility is 75 with a resonance frequency of 1.6 GHz

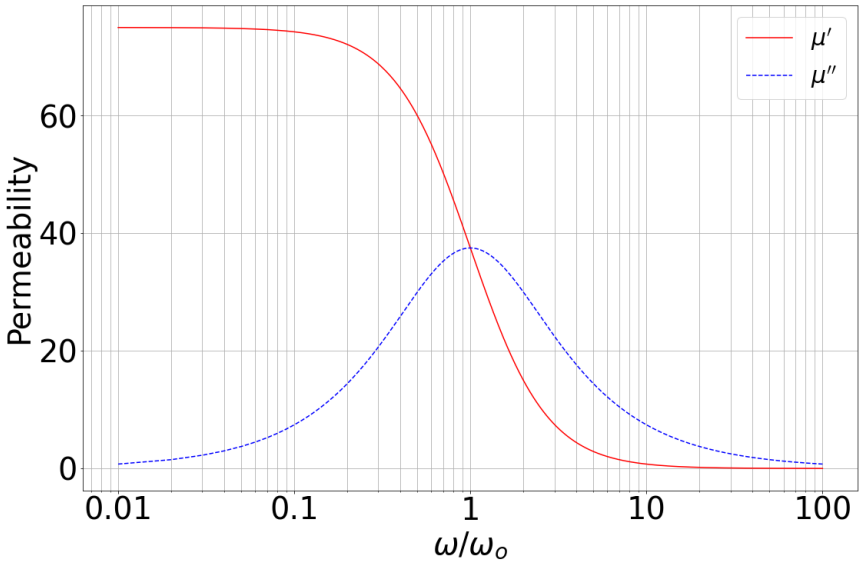

Figure 8: Single Debye permeability example. Initial susceptibility is 75 with a resonance frequency of 1.6 GHz

However, permeability still demonstrates a strong frequency dependence. Using Heaviside's formulation of Maxwell's Equations with the addition of magnetic conductivity it can be shown that magnetic conductivity is a function of permeable loss, $\sigma_m = \omega\mu_o\mu''$. Tom Sebastian coined the term Hesitivity (h_m) in his dissertation, which is the maximum magnetic conductivity of the material [1]. This maximum is assessed at the spectral maximum of the material making it a general property, similar to Snoek's product. Obeying the Kramer's Krönig relations enforces its utility even away from the peak loss.

The Debye model has a maximum conductivity that is twice the conductivity at the resonance frequency and the Lorentz model has a maximum conductivity equal to the conductivity at the resonance frequency. This relationship is shown below in Equations 20 and 21 [1]. This relationship between the magnetic conductivity and the permeability of a material is crucial for the developmental of Sebastian's new Hesitivity metric to be investigated next [1].

$$h_m(Debye) = 2\sigma_m(\omega_o) = \omega_o\mu_o(\mu_{DC} - 1) \tag{20}$$

$$h_m(Lorentz) = \sigma_m(\omega_o) = \frac{\omega_o\mu_o(\mu_{DC} - 1)}{\alpha} \tag{21}$$

2.4.1 Hesitivity

For materials obeying the Kramers Krönig relationship, the peak magnetic conductivity enters into the radiation efficiency equations in a form which masks its constancy. The functional form of f(μ) is a constant, for a Kramers, Krönig material. In the radiation efficiency Equations 13 and 15 a single value, hesitivity, determines the radiation efficiency a material can achieve in a loop or dipole configuration. The common part of each efficiency equation $f(\mu) = \frac{\mu''}{|\mu_r - 1|^2}$ can be written in terms of magnetic susceptibility, and Sebastian shows that this function $f(\mu)$ can be related to hesitivity strictly based on the DC magnetic susceptibility or permeability as shown in Equations 22 and 23 [1].

$$h_m(Debye) = \omega_o\mu_o\chi_{DC} = \omega_o\mu_o(\mu_{DC} - 1) \tag{22}$$

$$h_m(Lorentz) = \frac{\omega_o\mu_o\chi_{DC}}{\alpha} = \frac{\omega_o\mu_o(\mu_{DC} - 1)}{\alpha} \tag{23}$$

This relationship is related to the common value in the efficiency equations through $f(\mu) = \frac{\omega\mu_o}{h_m}$ with both Lorentz and Debye models reducing to the same value. Substituting in that relationship into the radiation efficiency equations leads to the conclusion that higher hesitivity increases radiation efficiency regardless of operating frequency as shown in Equations 24 and 25 [1]. Although other parameters may dominate the efficiency behavior, particularly at long wavelengths.

$$Eff_{dipole} = \frac{1}{1 + \frac{\omega\mu_o}{h_m} \frac{6}{\left(\frac{\rho}{l}\right)^2 (kl)^3}} \tag{24}$$

$$Eff_{loop} = \frac{1}{1 + \frac{\omega\mu_o}{h_m} \frac{12/\pi}{\left(\frac{\rho}{a}\right)^2 (ka)^5}} \tag{25}$$

The radiation efficiency of a magneto-dielectric dipole or loop antenna with a uniform current distribution can be determined by its physical dimension, operating frequency, and a single material parameter, hesitivity. Hesitivity can be calculated from the DC susceptibility or permeability, the resonant frequency of a material, and the relaxation coefficient for the Lorentz model [1, 9]. Electrical size and material selection dominate the radiation efficiency of MFC antennas.

This is, perhaps unexpectedly, convenient because most material data sheets don't publish the frequency dependent permeability or susceptibility for magnetic material, but rather the DC susceptibility or permeability. Similar to the Snoek product material families, hesitivity values allow engineers to select families of magneto-dielectrics for radiation efficiency without considering detailed dispersive data. To illustrate this point Figure 9, plots the radiation efficiency of five materials with known hesitivity for a common electrical sized application [1].

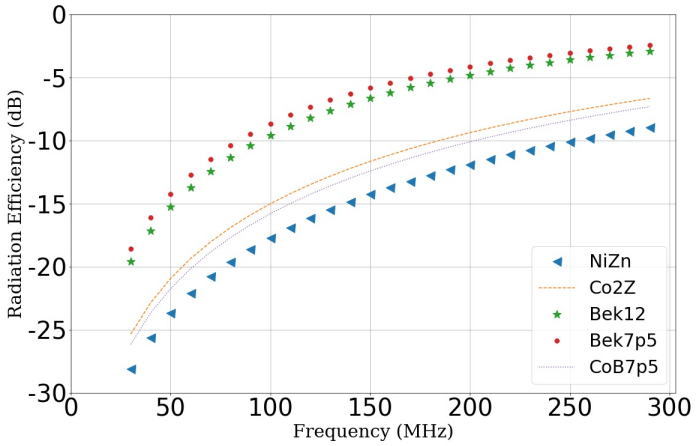

Figure 9: Radiation Efficiency of a 1 m cylindrical dipole with a .5" radius using different materials with their respective hesitivity in Ω/m: NiZn=55,240, Co2Z=104,200, Bek12=395,100, Bek7p5=501,00, and CoB7p5=86,400.

It is clear from Figure 9 that the materials with larger hesitivity demonstrate higher radiation efficiency all other variables are held constant. One thing to note with Figure 9 is that the frequency axis is fixed for all materials, so some materials are operating above or below resonance, outside the peak hesitivity point. It is not clear how far from the resonant frequency these materials can operate and still have the derived efficiency equations hold true because some materials are likely operating in different regions, which impacts the feasibility of producing the assumed uniform currents. With just the hesitivity parameter of different materials, derived from the DC magnetic susceptibility, the radiation efficiency of loop or dipole magneto-dielectric antenna can be predicted [1], under certain assumptions included in the analytic approximations.

Radiation efficiency isn't the only parameter that is important for antennas, but it provides a broad performance metric for magneto-dielectric materials as radiators. Sebastian postulated that the maximum bandwidth of MFCs are achieved when operating at the resonant frequency of the material, however, prior art and this in-

vestigation will support its modification to near the peak [1]. This simple design law aids material selection. In the next section, it will be discussed how magneto-dielectric wire antennas can be employed and the benefit they have over their metal wire antenna counterparts in conformal applications.

2.5 Value of Magneto-Dielectric Wire Antennas

Up to this point, only the possibility and viability of magneto-dielectrics have been considered in electrically small applications, but no basis for their use over other types of antennas was presented. This section documents and discusses the value and state of the art of MFCs. Among major design criteria such as form, fit, and function, form and fit are often traded against function. Specifically, the desire for smaller antennas constrains the form and fit driving metallic antennas to the limit of the electrically small regime where the previous derivations are based. Conversely, Figure 10 shows two metallic antenna examples, a blade antenna on the MQ-9 (left) [12] and a whip antenna on the Bradley (right) [13] in which function has been prioritized, of necessity, over a desirable form.

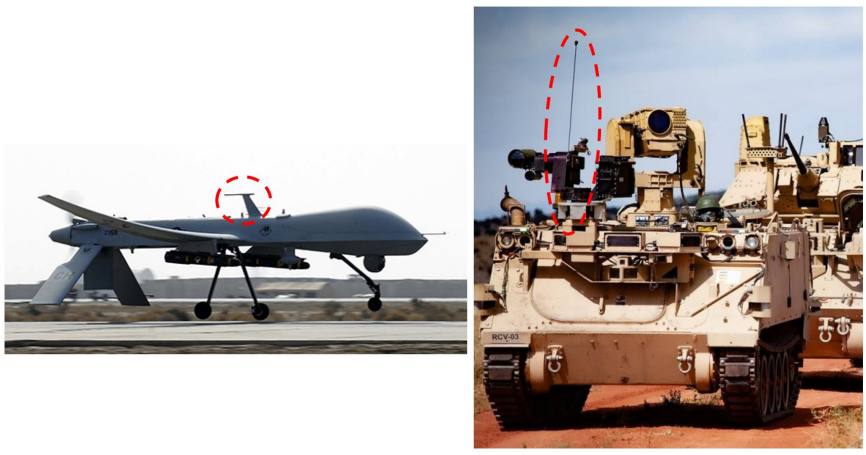

Figure 10: Both the blade antenna on an MQ-9 (left) and the whip antenna on a Bradley (right) are good candidates for replacement by MDWAs and MFCs.

The circled antennas in Figure 10, while effective antennas, are ill suited for their

environment. The blade antenna on the aircraft increases drag and its overall efficiency is reduced due to image currents along the aircraft skin in particular for the horizontal component. The whip antenna on the Bradley or similar High Mobility Multipurpose Wheeled Vehicles (HUMVEEs) can interfere with low obstacles, including power lines, and cause an electrocution hazard to the occupants of the vehicle. To increase vehicle mobility in urban terrain the whip antenna may be bent over and tied to the end of the vehicle again reducing efficiency due to the image currents produced on the skin of the vehicle. The image currents for metallic antennas are diagrammed in Figure 11, to demonstrate the cause of the negative impacts on radiation efficiency [14].

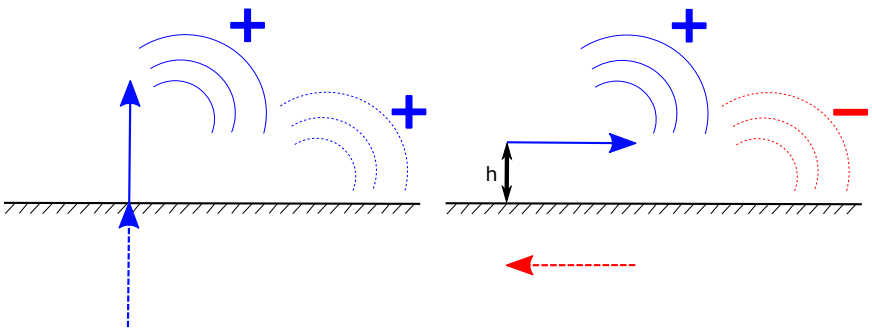

Figure 11: Image Theory Example with electric currents. Vertical currents (left) above a ground plane creates constructive interference. Horizontal currents (right) above a ground plane when the height, h, is less than $\frac{\lambda_o}{4}$ creates destructive interference.

Vertical currents above a ground plane are imaged in the same direction and constructively interferes with radiation. Conversely, horizontal currents above a ground plane are imaged in the opposite direction and when the height, h, is less than $\frac{\lambda_o}{4}$ it destructively interferes with radiation. The imaged current in the horizontal case limits how close a horizontal blade antenna can be to a ground plane, such as the skin of an aircraft and still have acceptable radiation efficiency.

In the case of magnetic currents as shown in Figure 12 the opposite is true. Horizontal currents placed directly on the ground plane produces an image current that

constructively interferes with radiation just as a vertical electrical dipole [10].

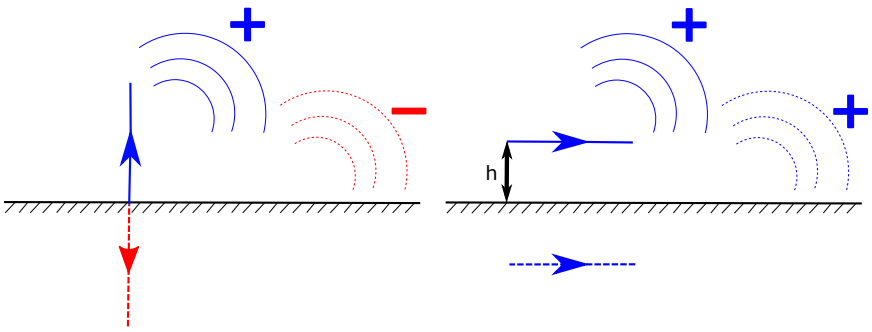

Figure 12: Image Theory Example with magnetic currents. Vertical currents (left) above a ground plane creates destructive interference. Horizontal currents (right) above a ground plane when the height, h, approaches 0 creates constructive interference.

This is the key performance drive for MDWAs and MFCs in conformal applications because when placed directly on the ground plane such as the skin of the aircraft or vehicle MDWAs benefit from full constructive interference from the image currents rather than the degradation experienced by metallic antennas. Given these advantages, some commercial MDWAs have been produced, leading to an evolving state of the art [15].

2.5.1 Current MDWAs

The two main MDWA designs that have been considered to this point are the dipole and loop configurations. The dipole configuration was fundamentally a stepping stone for MDWA development its key contribution was proof of the theory [1]. The magneto-dielectric dipole configuration produces a figure-8 azimuth pattern over a horizontal ground plane, which is the exact dual of an orthogonal metallic dipole. However, this isn't an optimal radiation pattern, which is a common design objective, for conformal antennas as it peaks only at broadside and nulls along end-fire. This case was considered first because of the duality between metallic, dielectric, and

magneto-dielectric dipoles allowed for a natural progression in the development of MDWAs.

Additionally, magneto-dielectrics are more difficult than electrical antennas to manufacture. Sebastian and *JEM Engineering LLC* created a NiZn ferrite tile dipole to validate the theory they developed [9]. The NiZn they used operated as an almost pure PMC with very low real permeability and relatively large imaginary permeability. Due to the high loss and low real permeability, the material is being operated in Region 1 of the three possible operating regions of magneto-dielectrics. NiZn is commercially available in rectangular tiles shapes lending itself to be used in a dipole configuration with minimal manufacturing risk. Figure 13, shows a model of the magneto-dielectric dipole antenna JEM produced using NiZn ferrite stacks, and driven by four uniformly excited feeds.

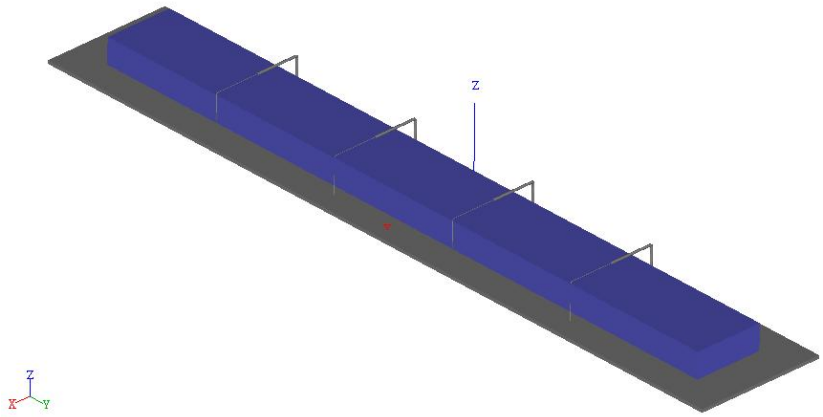

Figure 13: Model of the Magneto-Dielectric Dipole Antenna constructed by *JEM Engineering LLC* using NiZn ferrite tiles with four feeds.

This MDWA boasts a compact size of 40" long, 4" wide, and 1.5" tall. This small form is more impressive when considering the metallic antenna it was tested against. The comparison antenna was a metal monopole AS-3900 measuring approximately 9 feet in height, commonly referred to as a whip antenna [16]. This comparison isn't a strictly fair comparison because the whip antenna has an omnidirectional

horizontal radiation pattern while the magneto-dielectric dipole does not. However, it should be noted that even the specification sheet on RAMI's website for the AS-3900 makes reference to safety shielding protecting the users from overhead power line strikes and a max wind speed the antenna can operate in [16]. The small form of the MDWA mitigates both of those risks which is a key design element for the whip antenna, particularly for urban military applications. However, the AS-3900 weighs approximately 10 pounds. Metal antennas will in general be much lighter than magneto-dielectric antennas made of ferrites. The weight of the NiZn ferrite antenna shown was not disclosed, but it can be estimated to be between 165-185 pounds depending on the ratio type of NiZn they used from their supplier *Fair-Rite Products Corp.* [11, 17].

The operating range of the test was in the Very High Frequency (VHF) range, in particular the whip antenna has an operating frequency range of 30-88 MHz, over military VHF-low [9]. *JEM Engineering*, ASU, and Sebastian tested the MDWA against an AS-3900 whip antenna's frequency range. The MDWA was reported to perform as well or better than the whip antenna through the operating frequency of interest in its primary radiation direction. Additionally, the MDWA has an efficiency null near 110 MHz at which point the antenna is a half wavelength long, but restores gain after half a wavelength well beyond the electrically small limit this antenna was designed for [9]. So while successful, this design was not practical for specific ground vehicle applications.

In his dissertation Sebastian modeled a cylindrical loop antenna efficiency, but couldn't manufacture a viable material for a loop design. Several years after his dissertation another Arizona State University student, in partnership with *JEM Engineering LLC*, Tara Yousefi investigated the application of new highly permeable materials for wideband applications [18]. The main advancement between Sebas-

tian's dissertation and Yousefi's work was the introduction of commercial thin film permeable laminates, assessed to have high hesitivity. The thin film used was Cobalt-Zirconium-Niobium (CoZrNb) alloy deposited on a 12 μm thick film manufactured by *St. Gobain, S.A.*. This material exhibited two major features that enable alternative designs to the dipole. First CoZrNb has a much higher hesitivity than NiZn, nearly 7 times higher, even accounting for the laminated layering. Second, the laminate can be cut to a desired width and spooled around a core until the desired inner and outer dimensions are achieved, resulting in radially symmetric geometries at sizes not readily achieved by sintered ferrites.

The modeled toroid antenna shown in Figure 14 is constructed using spool wound CoZrNb thin film with a thickness of 2 cm, an outer diameter of 43 cm which was designed to operate from 200 to 400 MHz. It is mounted on a horizontal ground plane, with dielectric bands used to hold the wound laminate tight on a center hub. Four uniform feed loops similar to Sebastian's dipole antenna are used to generate a uniform current distribution throughout the toroid [18]. While this antenna geometry is electrically small in thickness, making it well suited for conformal applications, the outer diameter is approximately one third of a wavelength at 200 MHz. The total dimensions do not make this antenna strictly electrically small, but the small height above the ground plane is the key feature where MDWAs differ from and outperform their electrical counterparts.

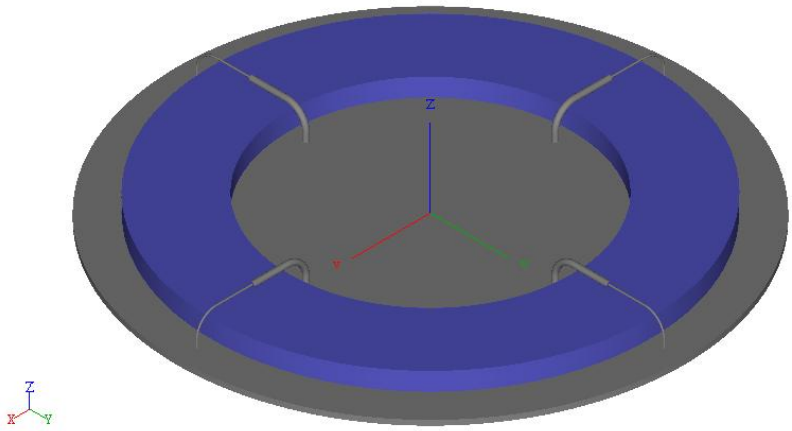

Figure 14: CAPSTONE model of Yousefi's toroid with ground plane and four feeds. This toroid design has radiation pattern benefits that the dipole does not.

Yousefi developed a radiation efficiency equation using the same derivation technique as Tom Sebastian to yield Equation 26 for toroids, where η is the impedance, a is the radius to the center of the toroid, k_o is the free space wavenumber, and Vol is the volume of the toroid, and h_m is the hesitivity [5]. This development is important because more feasible MDWAs can be designed using a toroid thin film design or ferrite stack dipole design. Additionally, she outlines the feed network connected to the four feeds and describes how the toroid antenna can be operated in two different modes, Mode 0 and Mode 1 each of which gives different radiation patterns. These should not be confused with the Transverse Electric (TE01) mode, but rather depending on how the toroid is fed it can be create a radiation patter similar to an electric dipole or a patch antenna for circular polarization [5]. This is a unique benefit enabling dynamic switching between radiation patterns to mimic two distinct metal antenna equivalents [19].

$$Eff_{toroid} = \frac{1}{1 + \frac{\eta 12\pi}{Volh_m}\left[(0.785a)^2 + \left(\frac{1}{k_o}\right)^2\right]} \tag{26}$$

Using this design Yousefi and *JEM Engineering LLC* were able to measure gain

ranging from -3 to +2 dBi from 200 to 400 MHz [18]. Except for being thinner in the vertical axis the overall dimensions are comparable to an electric dipole. However, in conformal applications the MFC provides a significant advantage over the electric counterparts in bandwidth.

As will be discussed in the next Chapter, Yousefi used the design laws Sebastian developed, but operated outside of the peak resonant frequency of the material. Her results still support the design laws, but the maximum bandwidth design law remained untested. The development up to this point has laid the foundation for the design laws that govern MDWAs under certain assumptions including uniform current, avoiding higher order modes, and physically realizable antennas which Yousefi summarizes [5]. In the next section we will address some of the modal analysis concerns that arise when dealing with high loss materials.

2.6 Modal Analysis of Magneto-Dielectrics

The crux of Sebastian and Yousefi's design laws is using a volume-based radiation efficiency equation. To use this equation several assumptions were made, with the most important being that the TE01 mode must be excited along the length of the MDWA. The feed structure is, as always critical to efficiently exciting the antenna. Sebastian used the coaxial feed shown in Figure 15 in his dissertation and dipole testing [1, 9].

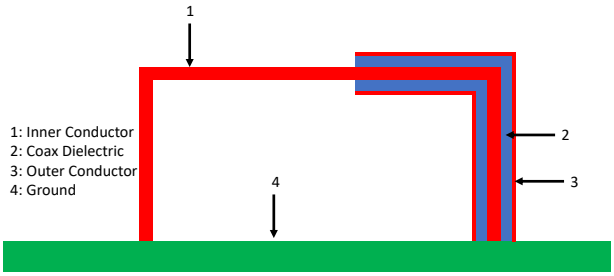

Figure 15: Cross sectional view of the feed to be used to excite the TE01 mode in the radiating structure. This feed structure generates uniform current along the vertical sections of the coax resulting in the TE01 excitation. The horizontal currents flow in opposite directions and negate each other.

This feed produces current on the inner conductor with an opposite current on the outer conductor. This feed generates current moving in the same direction along the vertical parts of the feed. The vertical currents excite a TE01 mode when driven at the appropriate frequency for the toroid cross sectional dimensions, but dependent upon field penetration. Moving further from the feed in the MDWA the TE01 mode will weaken due to the losses of the material. The second most important assumption the original authors' made was that the current is uniform throughout the MDWA. To force this condition multiple feeds were used in the dipole and toroid cases [9, 18]. This leads to a conflict between introducing loss for higher bandwidth and maintaining modal stability throughout the length of the antenna.

The original authors assumed TE01 mode, but did very little modal analysis work to support that claim. The cross section of the open dipole and toroid examples on a ground plane have no analytic solution for cutoff frequencies and modeling highly lossy materials presents additional challenges. The original authors commonly use a circular cross section cut off approximation, even though the actual geometries were

rectangular. A more detailed investigation of the modal implications of MDWAs operating near the material's resonant frequency is a key contribution of this thesis in the field of MDWAs.

III. Modal Analysis Improvements

Chapter II discussed the current state of the art for Magneto-Dielectric Wire Antennas. Sebastian's NiZn Ferrite tile antenna provided a proof of concept, and Yousefi applied Sebastian's design laws for material selection and volume based efficiency equations to develop the toroid design. Between Sebastian and Yousefi the published work has focused on the 30-400 MHz regime, but was most successful above 200 MHz [1, 5]. Their work showed that Magnetic Flux Channels (MFC)s can be manufactured and have several advantages over their metallic counterparts of the same size. First, the small size of MFCs, in key dimensions which can reach $\lambda/75$ in height are a critical advantage for conformal applications. Second, MFCs achieve high bandwidth due to loss in the permeability term than the same sized metallic antennas and not taking destructive interference loss.

Sebastian claimed that at the resonant frequency of the magneto-dielectric, the point of highest hesitivity, the largest bandwidth can be achieved, but did not support this with further modeling or measurements. The toroid design Yousefi implemented used CoZrNb as the permeable material with a resonant frequency of 1.5 GHz. Nonetheless, Yousefi's design ranged from 200-400 MHz, well outside the resonant frequency of the material operating in Region 3 low loss regime. Yousefi demonstrated the viability of her design at these lower frequencies, but did not explore the peak loss region. This also demonstrates the frequency independence of the hesitivity metric.

This work seeks to specifically address this band, for this material. Based upon the analytic design laws, Global Positioning System (GPS) is an application of interest that is centered in Region 1 of the material. In Figure 16, the real and imaginary parts of CoZrNb's permeabilty is plotted with GPS L1, L2, and L5 bands highlighted, using the Lorentz model from Chapter II. GPS is squarely centered around the resonant frequency of CoZrNb in Region 1 operation and provides a test of the design laws at

higher frequencies, whereas Yousefi operated well below resonance.

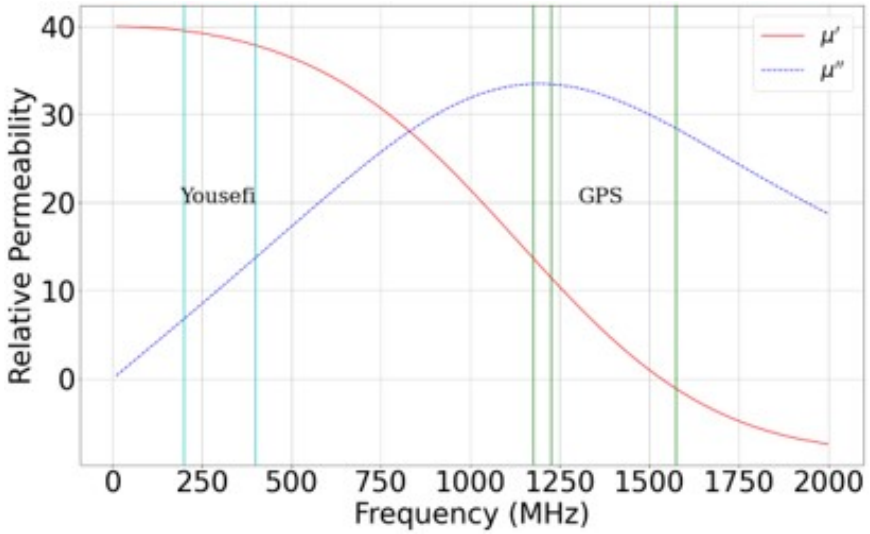

Figure 16: Yousefi used CoZrNb in her toroid design outside of the peak loss shown with the blue vertical lines indicating Region 3 operation. GPS is clearly centered on the peak loss of the material and provides a good use case as noted in the CoZrNb permeability figure for Region 1 high loss case.

The GPS band is taken as a use case in this work, but the goal is not to design an excellent GPS antenna. The frequency does not have the pressing electrical size challenges of VHF, a nd many other viable methods are available. Rather the goal is to test the compatibility of the design laws Yousefi and Sebastian have outlined at the peak hesitivity point of the material. To constrain the design the GPS antenna will mimic Yousefi's toroid with four feeds and will use the same CoZrNb material. This leaves several design parameters to be determined. As a reminder, Equation 27 is the radiation efficiency equation Sebastian developed for a toroid. The only geometric parameters this equation involves is an inner and outer radius, thickness, radius to the center of the toroid, and frequency.

$$Eff_{toroid} = \frac{1}{1 + \frac{\eta 12\pi}{Volh_m}\left[(0.785a)^2 + \left(\frac{1}{k_o}\right)^2\right]} \tag{27}$$

Applying this application near the peak hesitivity sets the center frequency, so the only parameters to be varied are the physical dimensions of the toroid. The coax feed itself introduces design constraints, but those are addressed in Chapter VI. Using Equation 27, Table 1 was generated. The first data column results in the same values Yousefi achieved in her design. The next three columns are notional antennas designed near the peak hesitivity of 1.5 GHz that achieve similar radiation efficiencies to Yousefi's toroid, which was taken as a benchmark.

Table 1: Radiation Efficiency of toroid antennas with varied dimensions and frequencies.

Parameter	**Yousefi Toroid**	**Case 1**	**Case 2**	**Case 3**
Frequency (MHz)	200	1500	1500	1500
Inner Radius (mm)	140	25.400	25.400	31.750
Outer Radius (mm)	216	50.800	50.800	44.450
Height (mm)	17.780	6.350	3.175	6.350
$\frac{\lambda}{height}$	81	31	61	31
Radiation Efficiency (dB)	-2.060	-1.530	-2.660	-2.660

The material dictates the center frequency and the manufacturing process imposes its own design constraints. Yousefi's toroid uses a spool wound magnetic film that reaches manufacturing limits as the film width diminishes. It is well known that a quarter inch wound tape is manufacturable and as thin as an eighth of an inch is able to be manufactured at scale, as demonstrated by audio cassette tapes [5]. Anything smaller than an eighth of an inch is taken as a physical limit that further constrains the manufacturability of the antenna and design process for this work. Using a quarter inch and an eighth of an inch thickness dictates how wide the toroid must be in order to achieve a given radiation efficiency, based on the volume dependent

efficiency equations. These two different heights still result in an electrically small thickness, of $\frac{\lambda}{height} = 31$ and $\frac{\lambda}{height} = 61$, making both of these viable options for electrically in height small antennas centered around 1.5 GHz. Cases 2 and 3 were specifically chosen because their volumes are identical leading to identical radiation efficiencies. This provides comparison cases for full-wave simulation to test the volume based design approach.

Another consideration, that isn't accounted for rigorously in the original work, is the modal implication of the design laws at higher frequencies. The premise of the radiation as posed by Sebastian and Yousefi is based on operating within the Transverse Electric (TE01) excitation, yet the frequency dependent permeability impacts the cutoff frequency for a fixed toroid size. Similarly, the modal structure of the excitation is based on the frequency dependent skin depth of the material. Operating at or near the material's resonant frequency may not allow the field to penetrate the material fully, resulting in different field structures than the desired TE01 mode.

The last major consideration in operating near the CoZrNb resonance is the constraint on the coax feed structure. The electrically small nature of the antennas and the feed structure presents a challenge for full-wave simulation. There is a fine line between the size of the mesh required to support the desired propagation and the smallest allowable mesh size before low frequency breakdown can be expected. The feed is further limited by the minimum bend radius of the coaxial cable selected, in particular for the appropriate semi-rigid types. As the size of the toroid is pushed smaller it presents physical limits on the spacing of coaxial cables to be used as feeds, impacting the input impedance of the antenna. Retaining the original feed loop construct imposes physical limits on how flat and small in loop width that the toroid can be made.

Based on these factors, this thesis will use the dimensions in Table 1 as a frame-

work to explore how the antenna behaves near the material's resonant frequency, using modal analysis techniques, 2D Finite Difference Time-Domain (FDTD) simulations, and full-wave simulations to understand the design laws' limits around the material's peak loss and across the different operating regions. The results lead to the extension of a trough design partially simulated by Yousefi which has different modal considerations and a different feed design that is less limiting than the coaxial feed.

3.1 Modal Analysis

Investigating the modal impact of operating at the material's peak loss is a critical point of evaluation for the design laws. The original authors spend a significant amount of time finding analytic solutions as an alternative to full-wave simulations that have significant computational cost. However, this process traded off certain accuracies and considerations for the speed and the insight of closed form solutions.

In this section, the assessment of the cutoff frequency for the TE01 mode for the antenna geometry will be investigated in more detail. For a rectangular cross section of magneto-dielectric on a finite ground plane, no analytic solution for cutoff frequency exists. This necessitates the use of simulations to find the actual cutoff frequencies, but some approximations can be made to select appropriate frequencies for testing. Underlying this entire analysis is the fact that an analytic mode may exist, and yet it may not be possible to efficiently excite it. This proves to be significant in the design process.

There are several useful analytic comparisons that can be made for the cross section of the toroid, but the most important is the infinite slab. The infinite magneto-dielectric slab in free space can be used to approximate what the TE01 cutoff frequency may be for a toroid of the same thickness. Balanis elucidates the well estab-

lished analytic cutoff frequencies for an infinite slab as shown in Equation 28 where h is the thickness of the slab, μ_d and ϵ_d are the relative permeability and permittivity, and μ_o and ϵ_o are the free space permeability and permittivity [10].

$$f_c = \frac{m}{4h\sqrt{\mu_d\epsilon_d - \mu_o\epsilon_o}} \tag{28}$$

Using Equation 28, the cutoff frequencies were calculated for the initial GPS toroid thickness. Figure 17 shows the change in cutoff frequency across the GPS bands.

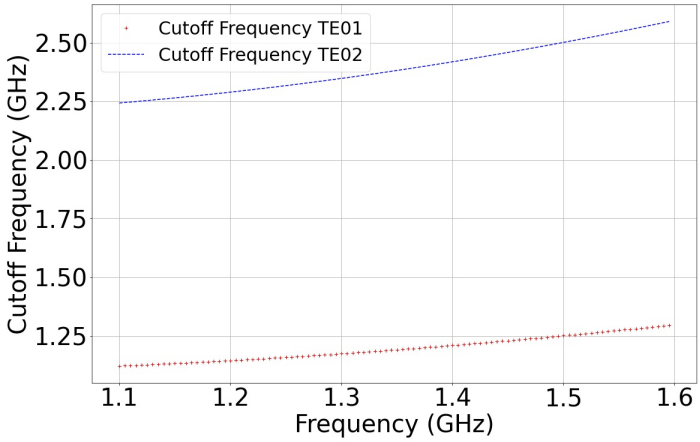

Figure 17: First two cutoff frequencies for an infinite slab a quarter inch thick. There is nearly a 300 MHz difference in TE02 cutoff across the range shown.

The key point in Figure 17 is that for the quarter inch thick slab the cutoff frequency changes significantly across the GPS bands due to dispersive constituent parameters. It should be noted, as Yousefi did, that the cutoff frequency for the quarter inch thickness of CoZrNb increases with frequency, which supports the antenna's ability to stay in TE01 in the GPS bands [5]. More specifically, this allows for the dispersive permeability and permittivity of a material to be leveraged for mode control of the antenna. Operating near the peak resonance allows for a larger bandwidth due to the frequency dependence of the modal cutoffs. This is just an analytic analogy

can only be taken as a guideline, as it does not fully represent the modal structure of the antenna. It does however, narrow the search for exact cutoff frequencies.

In her work, Yousefi avoided the peak loss of the material in her antenna design and almost no change in analytic cutoff frequency is observed across the operating frequencies. The comparison of analytic waveguides in the original toroid frequency band versus the peak loss band shows that the design trade becomes more complicated near peak loss.

Figure 17 demonstrates the impact of frequency dependent permeability on the TE01 cutoff frequency, but it doesn't show the impact of high material loss terms on the modal structure. To demonstrate this a skin depth calculation is presented for the magneto-dielectric material. Most skin depth calculations use an approximation using the conductivity of the material, but since this is an analytic equation the more rigorous form is shown in Equation 29. A skin depth calculation provides key insights into the limitations of traditional modal analysis operating near the peak loss of the material. Equation 29 is only frequency dependent due to the frequency dependence of the permeability.

$$SkinDepth = \frac{1}{\alpha} = \frac{1}{Re[j\omega\sqrt{\mu_o\epsilon_o\mu_r\epsilon_r}]} \tag{29}$$

However, examining the cutoff frequency and skin depth independently will not provide the insight, two metrics must be applied together. To facilitate this the independent variable is set as the thickness of the slab with the dependent variable being the cutoff frequency and frequency of that skin depth to produce Figure 18.

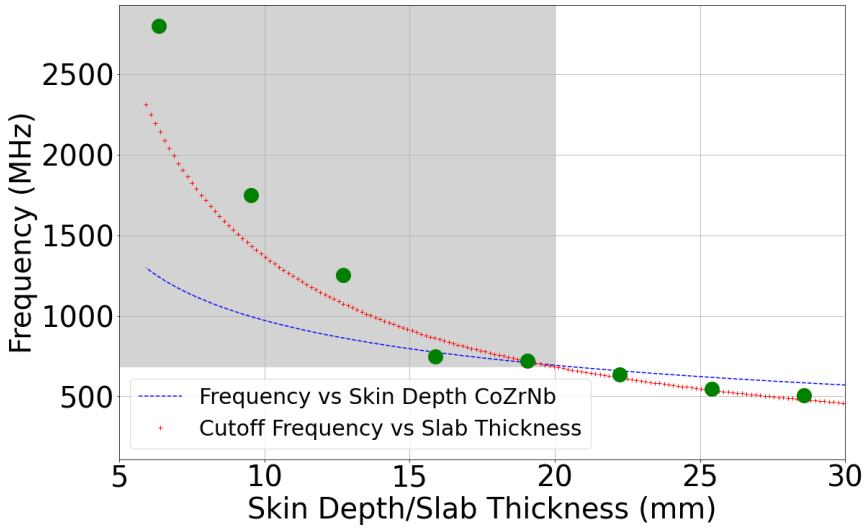

Figure 18: Skin depth (blue), analytic TE01 cutoff frequency (red), and TE01 simulated cutoff frequency (green) are all shown above. At larger thicknesses to the right of the shaded region indicates Region 3 operation where the infinite slab is a good approximation for the simulated cutoff frequency of the toroid. In the shaded area Region 1 operation begins to take over as the skin depth overtakes the thickness of the slab. This is where fields begin being pushed to the edge of the material indicating surface wave radiation.

The shaded region marks where the frequency of the skin depth is less than the cutoff frequency for the same size slab. In this region, losses begin to overcome the sought after TE01 field structure. The large circles in Figure 18 are the TE01 cutoff frequencies for toroids of the indicated thickness. These cutoff frequencies were found using an FDTD code Massachusets Institute of Technology Electromagnetic Equation Propagation (MEEP), which will be discussed in Chapter V. Examining the track of the green circles, points to several insights. The first is that the infinite slab cutoff frequency provides a good approximation of the cutoff frequency of the toroid when the cutoff frequency is less than the frequency for a full skin depth of the material. This is the Region 3 case Yousefi employed in the original toroid design. The second is that after that transition point to the shaded region, the cutoff frequency of the toroid is higher than the cutoff frequency of the infinite slab. These insights can help

identify where the the transition points between operating regions can lie.

Yousefi's slab was approximately 17 mm thick, which is just past the skin depth and cutoff frequency transition. She was operating her antenna well below the cutoff frequency where losses were minimal so there was no major concern with her excitation. Conversely, the quarter inch thick GPS antenna operates well below the cutoff frequency, but is centered around the 1/e skin depth frequency. Having a thickness equivalent to the skin depth doesn't mean there is no power penetrating the magneto-dielectric, but again it makes the design more complicated than Yousefi's case because the modal field distribution is perturbed. Even though the modal analysis to this point supports the volume based radiation efficiency design approach for Region 3 operation, Region 1 operation requires further investigation to determine the impact of the 1/e skin depth. This analysis helps identify transitions between the different operating regions. There is no analytic solution that can identify the modality of the toroid cross-section, but these two metrics offer some insight that can be supported with 2D FDTD analysis and full-wave simulations.

IV. Full-Wave Analysis

Using the prior art design process, based on radiation efficiency, the initial dimensions of a GPS were established [5]. The initial dimensions in Table 1 provided equivalent radiation efficiency compared to Yousefi's 200-400 MHz design. In the previous chaper it was shown that an infinite slab serves as an acceptable approximation for the TE01 cutoff frequency until the skin depth becomes smaller than the thickness of the toroid. This chapter uses a Full-Wave Finite Element/Boundary Integral method solver called Scalable Engineering Tools for RF Integration (SENTRi) to solve for the fields, radiation patterns, and scattering parameters. This process is very robust, but the geometry constraints creates some modeling challenges that will be discussed in Chapter VI.

Using a meshing and geometry tool called CAPSTONE the GPS antenna geometry in Figure 19 was created. It should be noted that the coaxial feeds are rounded at the corners of the feeds. The minimum bend radius for the specified coax is 0.75". The toroid itself is only 0.25" thick so this limits how close to the toroid the feed can be placed, based on the original toroid and feed design concept, this influences how well matched the input impedance of the toroid can be matched by the coax alone. Additionally, the bend may not support the desired field structure as well as more a vertical coax length on the sides of the geometry. This coax design will be investigated more in depth in Chapter VI. This chapter investigates the results of the full-wave analysis of the GPS toroid.

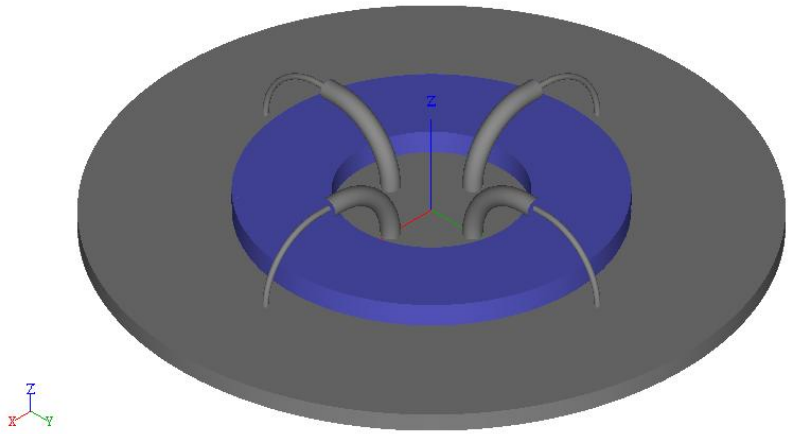

Figure 19: CAPSTONE model of the GPS toroid designed using Yousefi's design laws.

The GPS toroid design operating at 1.1-1.7 GHz mitigates mesh issues which must be addressed for lower frequencies in Chapter VI. Figure 20 shows the model's maximum gain at discrete frequencies and the radiation efficiency from Equation 27. It is important to note that gain and radiation efficiency shouldn't match because the modeled gain includes missmatch loss and directivity. The relationship between gain, radiation efficiency, mismatch loss and directivity (in dB) is shown in Equation 30, developed by Rothwell and Cloud [14].

$$Gain_{max} = eff_r + D_{max} - mismatch_{loss} \tag{30}$$

However, the trend of the gain and radiation efficiency plots should be similar based on the efficiency, but differ based on the directivity and mismatch. Assuming Mode 0 operates like an infinitesimally small dipole the directivity can be expected to be around 1.7 dB [20]. The full-wave simulated maximum directivity of this antenna is 1.3 dB indicating good agreement.

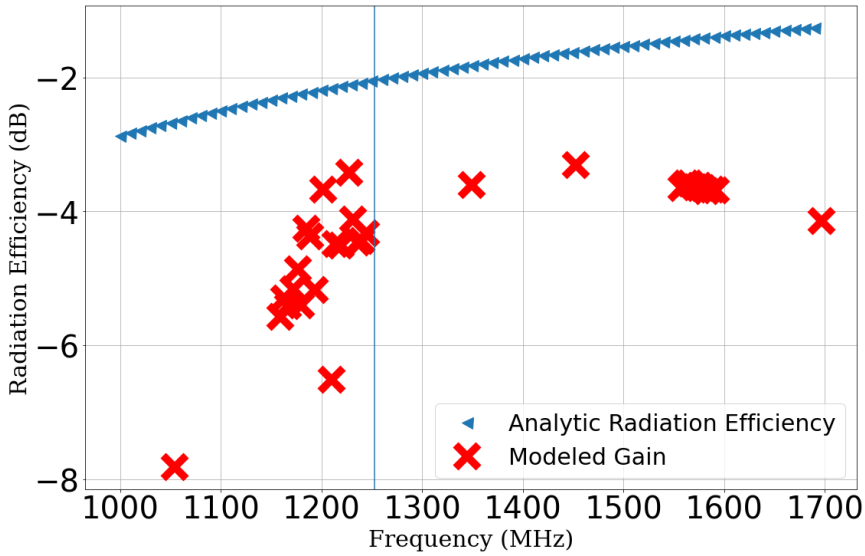

Figure 20: Gain and radiation efficiency of antenna case 1. This antenna was operated in Mode 0 (dipole equivalent) with all four feeds in phase. It should be noted that gain and radiation efficiency won't match because gain incorporates mismatch loss and directivity in addition to the radiation efficiency.

In Figure 20 the modeled gain is marked by the Xs and the analytic radiation efficiency by triangle marker. The vertical line marks the frequency that corresponds to the one wavelength circumference of the middle of the toroid. This initial design and feed structure has not been fully matched. So, better gain could certainly be achieved by adjusting the feeds,in fact the method employed by *JEM Engineering LLC* and Yousefi appears viable [19], but making a perfect antenna is not the goal. The goal is to study design law outcomes, when operating in the peak loss regime. There are several takeaways from this information. The first is that before the one wavelength circumference the gain is far worse than predicted by the radiation efficiency. This observation was also made by Yousefi in her work [5]. To mitigate this effect the toroid can be made slightly thinner, while shifting the radius to the center of the toroid further from the middle. That will keep the predicted radiation efficiency the same and push the one wavelength circumference below the frequency bands of interest in this case. This provides an additional case pointing to weakness in the

design laws, for which a simple rule inclusion would make their design law more robust.

The next major takeaway is that after the one wavelength point the gain is quite stable from 1.3 GHz to 1.7 GHz. It is also clear that while the analytic radiation efficiency tends to 0 dB at higher frequencies, that is not realizable. Yousefi discusses this point in her dissertation. The initial radiation efficiency equation by Sebastian was too optimistic at high frequencies by as much as 2 dB [5]. The conclusion she reached after developing the circuit model in Darlington form matches perfectly with the high frequency results which are shown in Figure 20.

Up to this point only mode 0 has been considered, in which all the feeds are driven in phase with each other which produces a dipole equivalent radiation pattern. The toroid design and feed setup has the benefit of operating in mode 1, which uses two feed pairs, with one pair 180 degrees out of phase with the other pair. The radiation efficiency equations derived by Yousefi for this mode is different than mode 0 and are shown in Equations 31, 32, and 33 [19]. This radiation efficiency equation is not volume based directly and does not indicate the possibility of achieving as high radiation efficiency as mode 0.

$$G_{rad} = Re\left[\frac{1}{\frac{3}{j\omega\epsilon_o a} + \eta\frac{3\pi}{4}}\right] \tag{31}$$

$$G_{loss} = Re\left[\frac{1}{j\omega\frac{\pi\rho^2\mu_o(\mu_r-1)}{\frac{a\pi}{2}}}\right] \tag{32}$$

$$eff_{M1} = \frac{Re[G_{rad}]}{Re[G_{loss}] + Re[G_{rad}]} \tag{33}$$

Exciting mode 1 mimics the directivity of a patch antenna. Based on Balanis' text, a patch antenna has a directivity of anywhere from 5-7 dB [20]. The maximum

directivity of this antenna operating in Mode 1 is 6.7 dB as expected by operating in mode 1. Figure 21, shows the modeled gain and analytic radiation efficiency. Note that the analytic radiation efficiency is different between mode 0 and mode 1, but not shown.

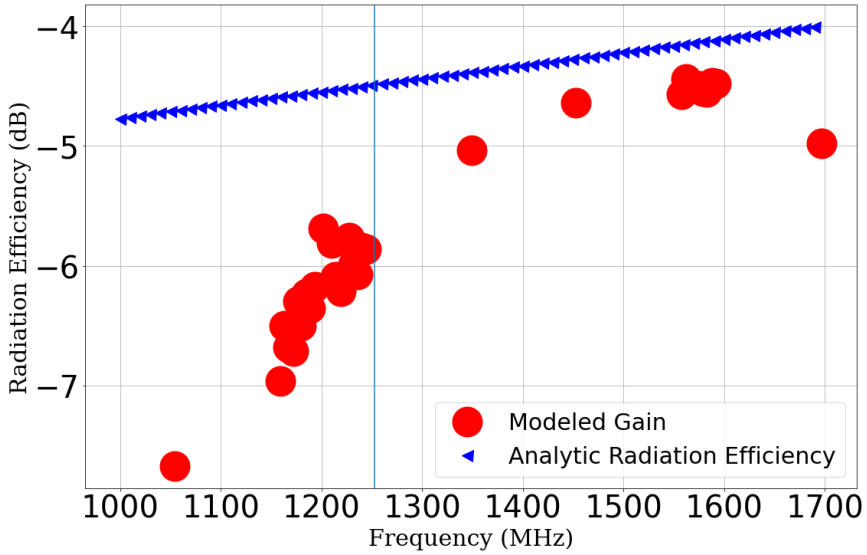

Figure 21: Gain and radiation efficiency of antenna case 1. This antenna was operated in Mode 1 (patch equivalent) with two feed pairs 180 degrees out of phase.

Even with lower radiation efficiency the gain is similar to between the two modes. However, the comparison is still not direct. The modeled radiation efficiency and analytic radiation efficiency can be compared by using Equation 30 and solving for the efficiency.

Feed matching is extracted from calculated port parameters predicted by the full-wave modeling and simulation. There are several common and important metrics that will be presented. The first is the Voltage Standing Wave Ratio (VSWR), the second is the reflection coefficient Γ, and finally mismatch loss. SENTRi post processing produces VSWR as an output. The reflection coefficient and VSWR could be calculated using the input impedance, but VSWR is a common metric for impedance matching. These are all well known functions posed in Pozar's Microwave Engineering

book among others [21].

$$|\Gamma| = \frac{VSWR - 1}{VSWR + 1} \tag{34}$$

$$MismatchLoss(dB) = -10log_{10}(1 - |\Gamma|^2) \tag{35}$$

Among all the frequencies investigated so far the best matches had a VSWR of 6.7 at 1.202 GHz, with the worst being 10.5 at 1.697 GHz. Those VSWRs respectively yield a mismatch loss of 3.45 dB and 4.98 dB. Clearly, without a specific matching network this is not good. Using the simulated mismatch loss, directivity, and gain the simulated radiation efficiency can be derived to compare directly to the analytic form Yousefi and Sebastian posed. The mode 0 excitation is shown in Figure 22.

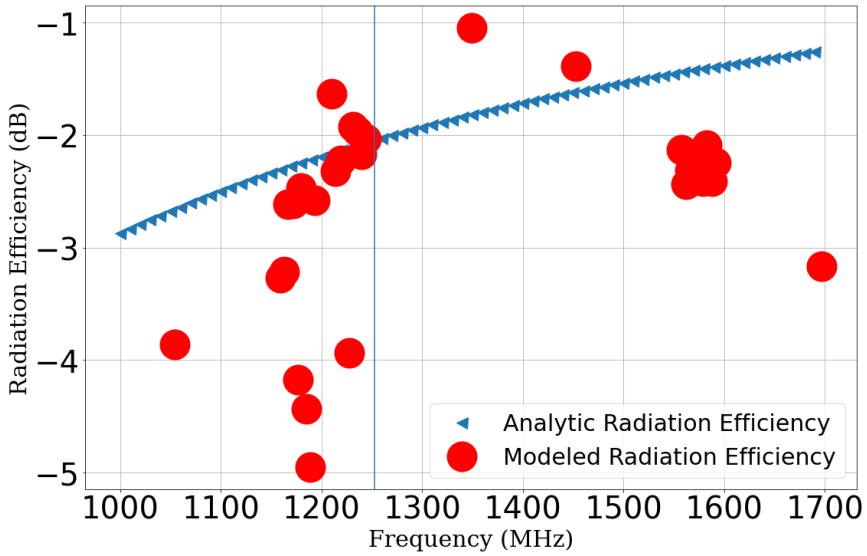

Figure 22: Modeled radiation efficiency and analytic radiation efficiency of antenna case 1 in Mode 0.

A matching network is strictly possible, and was used in the lower frequency toroid design. Therefore, it is reasonable to postulate its use, without including it in the FE/BI simulations. Comparing Figure 20 to Figure 22, it becomes clear that

the analytic radiation efficiency equation is close, but is still optimistic at the higher frequencies. The same estimate is applied for mode 1 results which are shown in Figure 23.

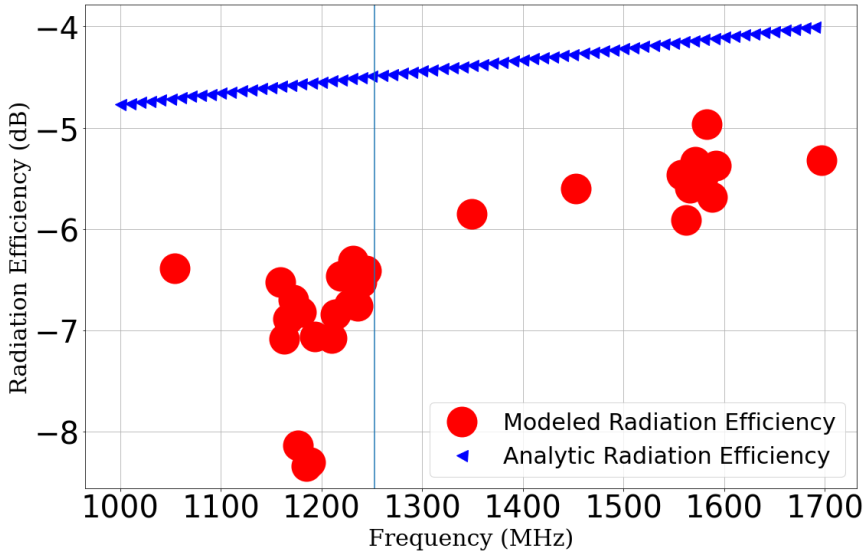

Figure 23: Modeled radiation efficiency and analytic radiation efficiency of antenna case 1. This antenna was operated in Mode 1.

The mode 1 excitation of this antenna has a radiation efficiency that matches the shape of the analytic radiation efficiency, but is nearly 2 dB less across the entire frequency band modeled. The overall effectiveness of the radiation efficiency equations based on volume generally support the original author's claim. While it does not yield a perfect match at the higher frequencies, it does provide a reasonable design point anchor.

Up to this point only one geometry has been tested. As a spot check a single frequency is modeled against both Case 2 and Case 3 from Table 1. Using the same method for Case 1 the modeled gain, directivity, and VSWR will yield the modeled radiation efficiency. This information is shown in Table 2 and the results follow the pattern of Case 1.

Table 2: Antenna case 2 and 3, modeled radiation efficiency vs analytic radiation efficiency of mode 0. These tests were operated at 1.176 MHz with no additional matching to improve the VSWR.

Parameter	**Case 2**	**Case 3**
Realized Gain (dB)	−5.730	−6.048
Directivity (dB)	1.025	1.210
VSWR	9.350	8.670
Mismatch Loss (dB)	4.570	4.310
Modeled Radiation Efficiency (dB)	−2.180	−2.950
Analytic Radiation Efficiency (dB)	−3.730	−3.730

Case 2 and 3 have the same material volume the analytic radiation efficiencies are identical. Case 2 uses a one-eighth inch thick toroid while Case 3 uses a quarter inch thick toroid that is half the width. Neither case matched the analytic equation perfectly, but are consistent with the wide band test of Case 2. This further reinforces the need for additional geometric design rules.

In summation, it has been shown that reasonable gain can be achieved even at the peak loss of the material using the design laws Yousefi and Sebastian postulated. However, the mechanism for the radiation mode is still unclear in this case, based solely on this analysis method. It is expected from prior art that the supported TE01 mode at low loss supports radiation, and when losses are large the field is pushed to the edge where radiation is supported by surface waves. When surface wave radiation is the dominant radiation mechanism, it should be expected that an efficiency calculation based on volume would over-estimate the radiation efficiency. Surface wave radiation would support the conclusion that at peak loss the volume based efficiency equation is optimistic because the whole volume is not contributing to the radiation [5]. This has significant implications to both Region 1 and 2 operation.

The next chapter examines how the losses impact the modal structure of the excitation as loss is increased in order to move towards refined design laws and recommendations.

V. 2D Finite Difference Time-Domain Analysis

No analytic modal solution for the toroid geometry exists, requiring a numerical solution by exact methods. For this thesis the code used is MEEP, which is an FDTD solver. MEEP was chosen because it has gone through rigorous solver validation and can easily incorporate anisotropy that these materials possess, though it is not investigated in this thesis. Furthermore, the code implementation is amenable to 2D cross section work. The toroid design, with high loss CoZrNb magneto-dielectric has a low resonance Q factor so care has to be taken to excite the desired modes. It was established in Chapter III that the infinite slab waveguide analytic solution is a useful guide for initial cutoff frequency estimation.

The use of lossy materials is generally avoided for waveguides and resonant structures. Traditionally for wave guides and resonant structures loss is avoided, so the excitation is simple and propagation long. This is in line with earlier ferrite work as well. A simple Gaussian pulse can cause resonance in the structure and a measurement can be done several periods after source turnoff to find a steady state solution. Operating at the peak loss of the material, this type of excitation may not suffice as the decaying field may not persist sufficiently long to isolate the modal structure. To test whether a Gaussian pulse would suffice in a high loss environment, the lossless case was first investigated, to see the expected TE01 mode without loss. In Figure 24, the quarter inch thick toroid is excited using a Gaussian pulse into the page, z-directed, at 1.3 GHz. At this frequency, the material has a permeability of $\mu = 9 + 35j$, but the magnitude was taken for the lossless case leading to $\mu = 36.05$.

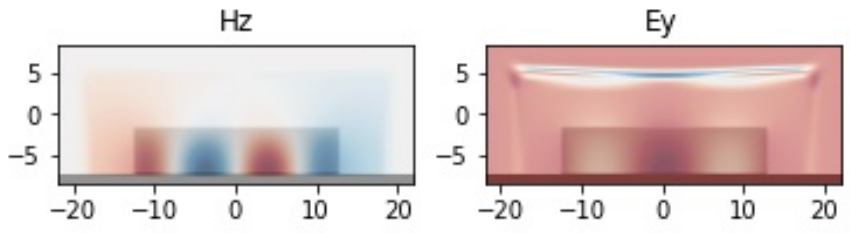

Figure 24: Relative normalized field strength of Hz and Ey based on the Hz Gaussian excitation at 1.3 GHz. The material properties used are $\epsilon = 3$ and $\mu = 36.05$. The expected TE01 excitation is achieved and shown by the dark red region in middle of the Ey field.

This test produced the expected field structure for a grounded, lossless, rectangular wave guide. A TE01 mode is present with no loss, but as loss is added the mode is expected to become more difficult to isolate. Rather than moving directly to the final permeability of the material an intermediate loss case, $\mu = 35 + 9j$ with the same magnitude was evaluated and the results are shown in Figure 25.

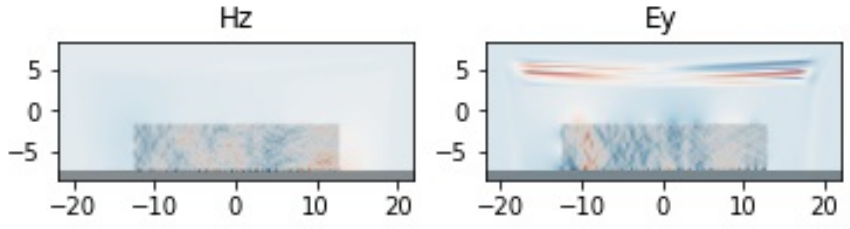

Figure 25: Relative field strength of Hz and Ey based on the Hz Gaussian excitation at 1.3 GHz. The material properties used are $\epsilon = 3$ and $\mu = 35 + 9j$. No visible excitation survived the high loss.

It is clear that even with a moderate loss, well short of the desired loss, that the Gaussian pulse excitation cannot support field structure in the material. The results reveal that, there are two major problems with this simulation method. First, the Gaussian pulse is not able to establish fields that last long enough to be measured in a high loss environment. To mitigate this a continuous source must be used. A continuous source uses a much more narrow band excitation so finding the resonant frequency

requires more discrete searching, but provides enough excitation to overcome the loss of the material.

The second problem is the type of modeled excitation. The first few simulations used a point-field source inside the medium, but the large permeability results in a high impedance difference at the material interface and sourcing from inside the medium doesn't provide a realistic model of the feed structure. Current sources outside of the medium more directly model how the coax feed structure will interact with the impedance boundary to establish the fields inside the medium.

However, the continuous source presents a challenge for evaluation. The source is active at the time of evaluation and presents the strongest return, which dominates the data scale for the field. To mitigate this the plots scales have been adjusted to show field structure only, but the strength of the return is visually over-saturated. To make sure the continuous wave source behaves as expected the lossless case at 1.3 GHz is shown in Figure 26.

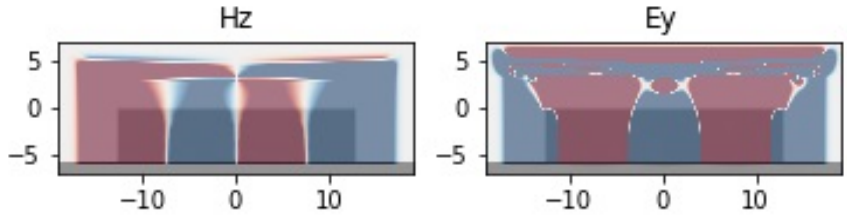

Figure 26: Relative field strength of Hz and Ey based on Ex and Ey current excitations at 1.3 GHz. The material properties used are $\epsilon = 3$ and $\mu = 36.05$. The expected TE01 excitation is achieved and will support the postulated radiation mode.

This is the same result as with the lossless Gaussian pulse as expected. To demonstrate how losses impact the field structure incremental loss is added starting with $\mu = 35 + 9j$, as shown in Figure 27.

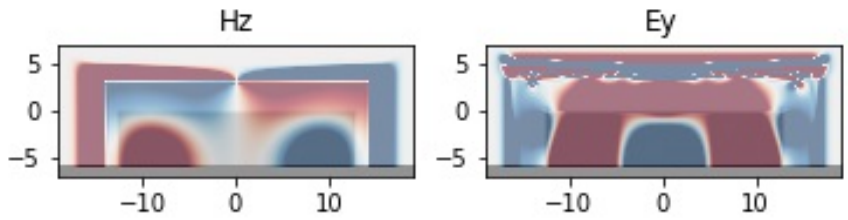

Figure 27: Relative field strength of Hz and Ey based on Ex and Ey current excitations at 1.3 GHz. The material properties used are $\epsilon = 3$ and $\mu = 35 + 9j$. Expected TE01 excitation is achieved, but penetrates less volume than the lossless case.

With a moderate amount of loss added it is clear that the TE01 field is still supported by the continuous wave source. It is also observed that the field is reduced after the loss is added when compared to the lossless which is of course as expected. Adding even more loss so that the permeability is $\mu = 30 + 20j$ results in the field distribution shown in Figure 28.

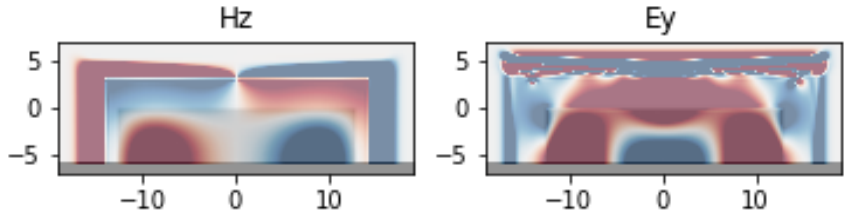

Figure 28: Relative field strength of Hz and Ey based on Ex and Ey current excitations at 1.3 GHz. The material properties used are $\epsilon = 3$ and $\mu = 30 + 20j$. Expected TE01 excitation is achieved, but utilizes less volume than the less lossy case.

As the loss is increased the ability of the continuous wave source to penetrate the medium is decreasing, stated another way, the skin depth is approaching the dimensions of the geometry. To show what field distribution could actually be achieved at this frequency the permeability must be adjusted to $\mu = 9 + 35j$, and the results are shown in Figure 29.

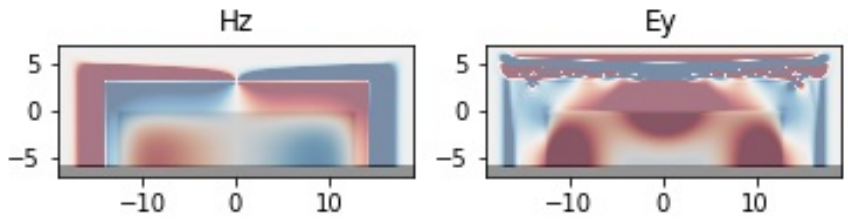

Figure 29: Relative field strength of Hz and Ey based on Ex and Ey current excitations at 1.3 GHz. The material properties used are $\epsilon = 3$ and $\mu = 9 + 35j$. TE01 excitation is no longer present, due to high loss.

At this high of loss the majority of the field has been pushed to the edge of the medium, indicating surface wave radiation. There is no longer a viable TE01 mode established in the medium rather a surface wave mode about the boundary. The original authors postulated that the TE01 mode was the desired radiating mechanism and built their design laws around that construct. This was certainly true in their operating frequency for the material used because the permeability was still low loss. As the operating frequency approaches the peak loss of the material the losses become too large to support an internal TE01 mode and must transition to a surface wave radiation mode, which was postulated by Sebastian in his Perfect Magnetic Conductor (PMC) case [1].

Surface wave radiation significantly impacts the size reduction which antennas can achieve. The size of the antenna is no longer dictated by establishing an internal TE01 mode, therefore the material adjusted wavelength isn't a factor in reducing antenna geometry dimensions.

The transition to surface wave radiation is in line with the limiting case of Yousefi's use of loss to manipulate the cutoff frequencies, and also in line with what is observed in MEEP simulations. In Figure 18 the shaded region where the skin depth frequency was less than the cutoff frequency and in Figure 16 where the imaginary part of the permeability becomes larger than the real part both occur between 700 and 800

MHz. These two metrics can be used to identify where the radiation mechanism transitions from TE01 to surface wave. Coupling 2D FDTD simulations with skin depth and analytic cutoff frequency approximations can indicate transitions between the different operating regions.

In Figure 20, the full-wave model is operating at a higher frequency where surface waves are expected and there is still significant radiation efficiency from the surface wave radiation mode. The original authors used a radiation efficiency calculation that was based on the volume of the toroid. Due to the surface wave radiation the full volume of the toroid is not being utilized for radiation and a volume based approach is not well suited. Yousefi in her dissertation partially corrected the radiation efficiency equation via the Darlington Form circuit model and the new radiation efficiency equation changed from Sebastians' original [5]. The new form is shown in Equation 36.

$$eff = \frac{1}{1 + \left[\frac{3\pi}{8ka\left(\frac{\rho}{a}\right)^2} + \frac{1.89}{(ka)^3\left(\frac{\rho}{a}\right)^2}\right]\left(\frac{\mu''}{[\mu''-1]^2+\mu''^2}\right)} \tag{36}$$

Using the Darlington Form more accurately depicts the radiation efficiency at higher frequencies by modifying the electrical length scaling and incorporating the circumference of the toroid not the volume.

This more accurately represents the high loss surface wave radiation that is physical to Region 1 operation. This is still a rough estimation because Yousefi is still using a circular cross section instead of a rectangular cross section and does not distinctly acknowledge skin depth factors. Calculating the skin depth of the material and doing a size comparison with the anticipated dimensions from the prior art design laws can help identify the antenna's operating region. The new efficiency equation is still an approximation, but provides valuable insight into the toroid antenna design at

low computational cost before transitioning to a full wave method for further design development.

VI. Meshing and feed requirements

The original authors experienced difficulties modeling their antennas, most of their challenges were centered around the feed structure and will be investigated in this chapter. Developing an appropriately sized mesh for antenna modeling is challenging for traditional antennas where features span electrical size regimes, but becomes increasingly more challenging for conformal Magneto-Dielectric Wire Antennas (MDWA)s. The scale of the problem is bested considered in wavelengths. At 1.5 GHz the relative wavelength in the CoZrNb medium is about 10 times smaller than the free space wavelength. This compacts the freespace wavelength of 20 cm down to 2.1 cm in the medium. For computational solutions for electromagnetic problems a general rule of thumb for mesh sizing is to have at least 10 meshes per wavelength and the requirement can be much higher for resonant, modal and sharp features as discussed by Warnick [22]. This creates a mesh size of nearly 2.1 cm being required throughout the entire medium. This requires a single edge along the outside of the toroid to require 76 meshes. Volume meshing the entire surface and interior region creates an even larger problem for modeling. Even though the mesh required to accurately model the toroid is large, it can be handled by high performance computing resources. The real challenge appears in the feed structure meshing for this particular feed geometry.

Coaxial feeds are typically short, running just far enough to reach the radiating element with the center conductor. Additionally, the dielectric material doesn't extend past the ground plane so only the center conductor is in the modeling region. With the feed structure used for the toroid the relatively low dielectric of the coax is present in the model and very electrically small compared to the operating frequency. The toroid design utilizes four such feeds instead of one so the challenge is compounded.

The coax that was selected for this case is from Pasternack with specifications of

semi-rigid coax cable with inner conductor diameter of 1.63 mm and outer conductor diameter of 6.35 mm [23]. This coax was selected because it is approximately 66 percent larger than a traditional RG-6 coax. The larger size coax used here has a minimum bend radius of 0.75", which is another physical limit in this design. The ability to bend the coax and the size of the coax all influence the viable operating frequency and the ability to build and model the feed structure. Most importantly the size of the coax feed and spacing can dramatically impact the input impedance. A larger coax is easier to match at lower frequencies, but the physical constraints of a larger coax can prevent ideal placement to include potentially not even being spaced closely enough to aid impedance matching.

The feed structure provides a significant amount of volume that needs to be meshed. The challenge with the coaxial feed is that typically the operating frequencies are much higher than the ones implemented for MFCs. Low frequency breakdown is a phenomenon common in all full-wave electromagnetic solvers. It is especially important to consider when dealing with electrically small structures. SENTRi flags potential low frequency breakdown when the smallest mesh is less than $\frac{\lambda}{1000}$ of the longest material adjusted wavelength. The coax feed to be employed is very electrically small compared to the operating frequency of Yousefi's toroid design. Essentially, with low frequency breakdown the mesh is too fine with respect to wavelength to solve Maxwell's Equations within the precision of the machine where the phase propagation breaks down.

The size of the coax is important when setting the meshing requirements. It was determined that the toroid requires a mesh of 2.1 cm, but that mesh size would vastly under mesh the port faced used in this excitation. Figure 30a shows how an even smaller mesh of 2.1 mm could not support a proper port excitation, let alone allow the excitation to travel accurately to the end of the coax dielectric.

A trade off must be made between the mesh required to excite the port properly and avoiding low frequency breakdown. It should be noted that the center conductors in Figures 30a and 30b are not filled with a volume to reduce the model size. The center conductor is being modeled as a Perfect Electric Conductor (PEC) which has a skin depth of zero so only the surface has to be meshed. SENTRi provides documentation of appropriately sized meshes for coaxial feed structures. Figure 30b shows what might be considered an appropriate mesh, which is 0.25 mm as the smallest size.

The 0.25 mm sized meshing provides the necessary field structures to use the coaxial cable as a feed, but it pushes the mesh sizing well below the potential for low frequency breakdown at Yousefi's frequencies. At 200 MHz a 0.25 mm mesh has a mesh size to wavelength ratio of around $\frac{\lambda}{5500}$. To operate outside of the potential for low frequency breakdown the lowest possible modeling frequency is near 1.1 GHz. To

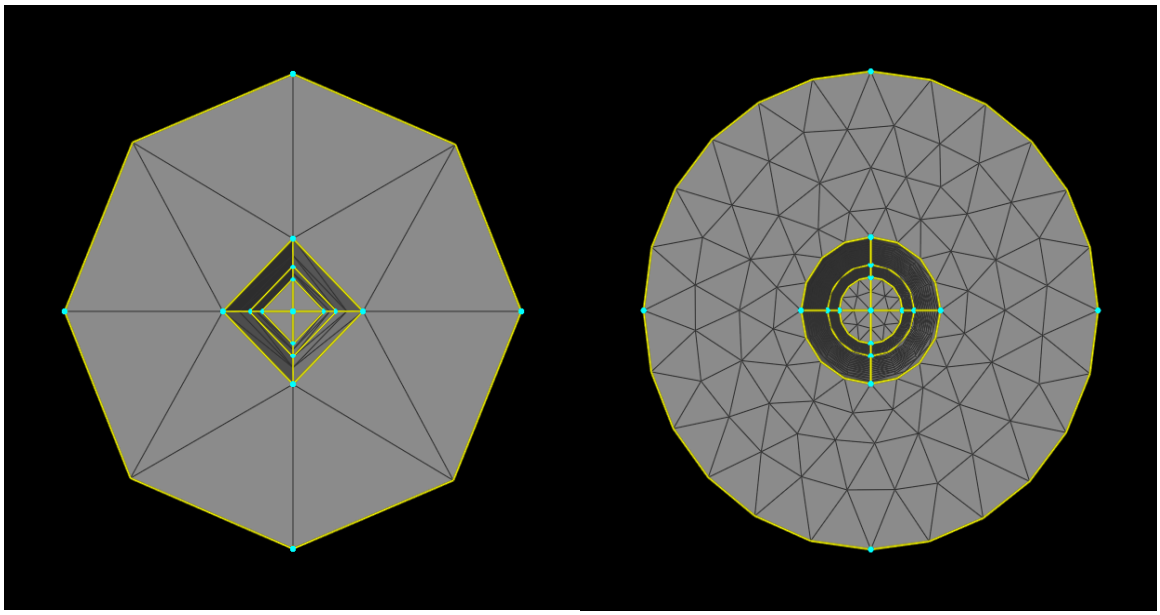

(a) Mesh structure with a 2.1 mm mesh sizing. Would not support a Transverse Electric and Magnetic (TEM) wave in this coax.

(b) Mesh structure with a 0.25 mm mesh sizing. This would support a TEM wave in the coax.

Figure 30: Different mesh sizing demonstration for low frequency breakdown.

test for and show the impact of low frequency breakdown a coax stub shown in Figure 31a is modeled with varying mesh sizes and frequencies. The short stub is a poor radiator, but demonstrates the effect of low frequency breakdown in the radiation pattern.

Setting the minimum mesh size as 0.25 mm allowed the meshing tool to create a mesh size of 0.272 mm. Using that mesh a test at 1.1 GHz was conducted and produced the expected radiation pattern shown in Figure 31b. Testing the same mesh at a lower frequency demonstrates the low frequency breakdown effect. Figure 31c uses the same mesh excited at 200 MHz.

It is clear that low frequency breakdown creates an uneven distribution indicating non-physical results. Using this mesh sizing at 200 MHz, the feed would perpetuate non-physical results into the antenna modeling. The original authors did very little

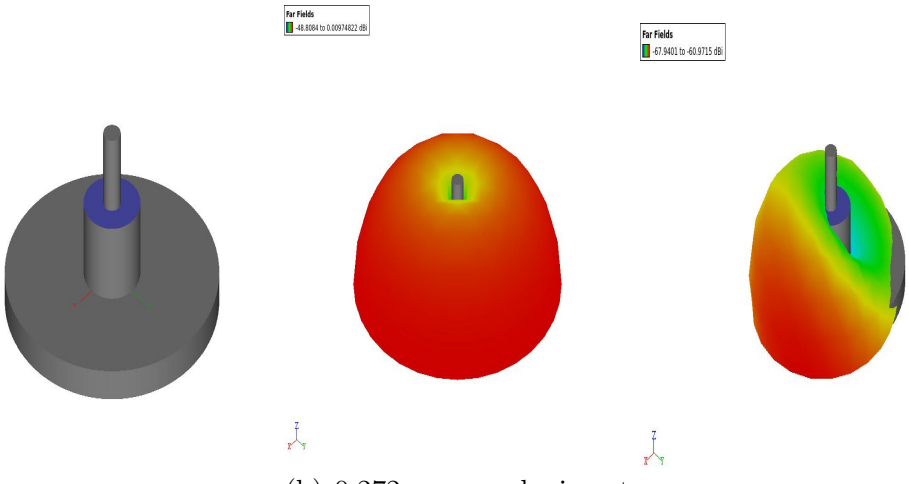

(a) Stub radiator simulation setup.

(b) 0.272 mm mesh size at 1.099 GHz. Demonstrates expected uniform radiation pattern without low frequency breakdown.

(c) 0.272 mm mesh size at 200 MHz. Demonstrates low frequency breakdown's impact on radiation pattern.

Figure 31: Demonstration of low frequency breakdown's impact on radiation pattern the stub radiator radiates poorly, but uniformly. With no low frequency breakdown the radiation pattern is uniform, but below the low frequency breakdown threshold the radiation pattern breaks down and is no longer uniform.

modeling and simulation work for their antennas at low frequencies because the feed structure requires such a dense mesh. This is likely one of the reasons they focused on closed form approximations to anticipate a result even though modeling their antenna was not feasible. Even using high performance computing clusters with a mesh size that would both support the port excitation and avoid low frequency breakdown, the state of the art computational resources could not handle the mesh size at their lower frequencies. While this precludes a piece of touchstone work with prior art, the intended analysis can continue due to the differing operating frequency. This is indicates that the low operating frequency isn't just a modeling issue, but a physical size disconnect between the feed and the antenna.

For the purpose of this thesis the peak loss of the material is being investigated around GPS frequencies. Operating the same coax feed above 1.1 GHz avoids low frequency breakdown. Additionally, the higher frequency leads to a smaller length of coax that requires meshing, which allows the GPS toroid to be solved using full-wave simulations. A smaller sized coax could be considered with a smaller minimum bend radius, but that would require smaller mesh sizing so that each individual mesh would need to be tested for low-frequency breakdown. That would also potentially make the mesh too dense to run even with high performance computing resources. Additionally, the feeds are exposed by protruding above the antenna and ground plane, making them susceptible to damage in certain environments. These results suggest that an alternative feed structure is desirable, and one is examined in Section 7.2.

Several individual antenna cases have been investigated, but the considerations across the operating regions have yet to be addressed. Chapter VII will address these different operating regions before alternative antenna designs will be considered in Section 7.2.

VII. Permeable Antenna Operating Conditions

There are three main regions associated with permeable antennas based on the permeability of the material being employed at a specific frequency. Region 1 is the frequency range where $\mu'' > 2\mu'$, Sebastian's NiZn dipole operated in this region from 30-88 MHz with low real permeability and imaginary permeability. Region 2 is the frequency range where real permeability and imaginary permeability terms large and roughly the same, none of the work to date has operated in this region. Region 3 is the frequency range where $2\mu'' < \mu'$, this is where Yousefi's CoZrNb dipole operated in the 200-400 MHz region. The GPS toroid designed in this work operated from 1.1-1.6 GHz with high losses or imaginary permeability and low real permeability placing it in Region 1. Figure 32 shows the relationship between CoZrNb's permeability and efficiency using Equation 8, with the electrically size factor removed.

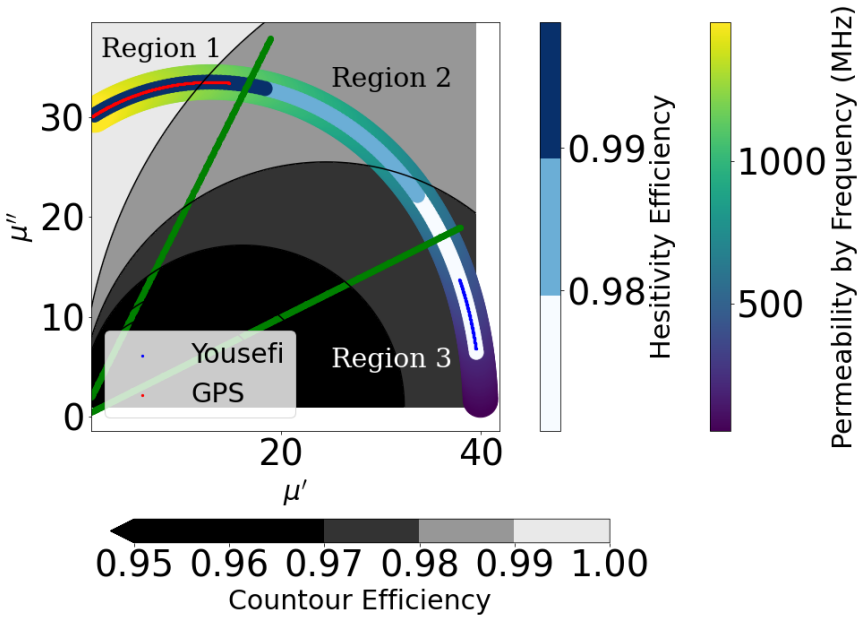

Figure 32: Radiation efficiency contours of a toroid, shown in gray shaded regions, based only on permeability not size. The purple, blue, and yellow arc is where the CoZrNb would be based on it's permeability at a given frequency. The green lines indicate the transition lines from one region to the next. The red arc shows the GPS operating frequency of CoZrNb, indicating Region 1 operation, while the blue arc shows Yousefi's operating frequency of CoZrNb, indicating Region 3 operation. The dark blue, light blue, and white arc shows how hesitivity approximation in Equation 24 at a given frequency aligns with the permeability based efficiency of Equation 8.

In Figure 32 the operating regions are divided by the green lines and the hesitivity based efficiency aligned with the permeability based efficiency contours. The GPS sized toroid operates in Region 1, marked by red, while the Yousefi toroid operates in Region 3, marked by blue. This is the same material operating in two very different radiation modes.

It was observed in MEEP through modal analysis that operating in Region 3 allows an established TE01 mode to develop, while operating in Region 1 forces the fields to the surface of the material resulting in a surface wave radiation mode. Operating in Region 1 supports the maximum bandwidth of operation, where the losses are broadly the highest, at the highest hesitivity. The max bandwidth at higher losses

near resonance works regardless of antenna type, but is widely applicable to the materials and orientations desired in the magnetic flux channel concept [5].

The hesivitity based radiation efficiency arc is more optimistic than the permeability based radiation efficiency because it is missing the frequency dependent permeability actually present at the operating frequencies. Hesitivity is a great tool to find and select classes of materials with the highest hesitivity because higher hesitivity will in general lead to increased radiation efficiency.

The permeability based radiation efficiency calculation obscures the impact permeability has on radiation efficiency because it is frequency dependent, but is more accurate than the hesitivity equation alone which lacks a frequency dependent term. In general, a class of material should be chosen with the highest hesitivity, then the material within that family with the peak resonance closest to the desired operating frequency should be selected. Once a material is selected the radiation efficiency calculation should be completed using the permeability based radiation efficiency. In prior art the hesitivity based radiation efficiency was mostly used, extending their design laws the permeability based radiation efficiency should be used after material selection.

7.1 Hesitivity Limitations

The value of finding a material with the highest hesitivity is especially important to reduce the size of overall antenna dimensions to achieve the same radiation efficiency, but has certain limitations in its applicability as well. Sebastian designed his NiZn dipole to operate from 30-88 MHz, with the dimensions being 40 inches long, 4 inches wide, and 1.5 inches tall [1]. The hesitivity of NiZn used was approximately 55,400 Ω/m and operated in Region 1 with high loss and low real permeability. The permeability of NiZn is shown in Figure 33. If CoZrNb were to be packed into a trough

dipole configuration instead of a toroid, with a hesitivity of 346,000 Ω/m [5] a dipole 6 times smaller in volume would achieve the same radiation efficiency regardless of the values for permeability according to the hesitivity based radiation efficiency equations. CoZrNb operating from 30-88 MHz would be operating well below Yousefi's frequency and is still in Region 3.

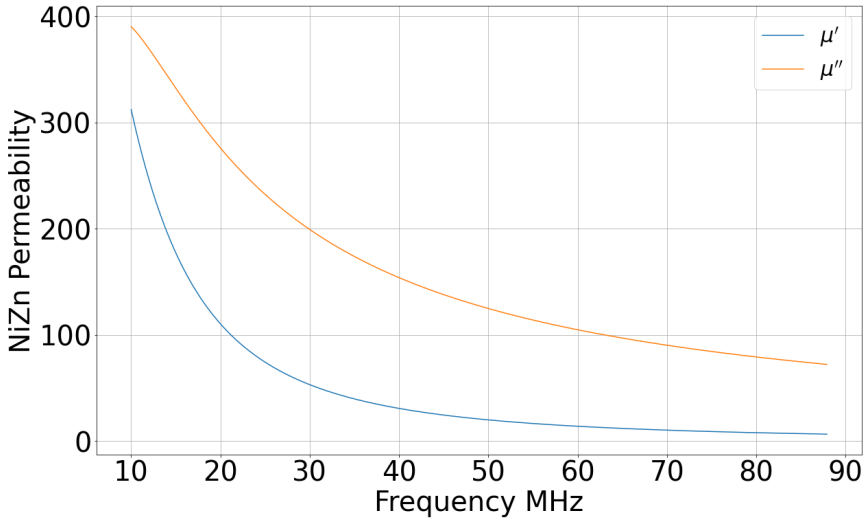

Figure 33: NiZn permeability across Sebastian's dipole frequency range. The high loss indicates this antenna would be operating in Region 1, the highly lossy case.

This would result in reducing the size of the dipole to 20 inches long, 2 inches wide, and 1 inch tall, using CoZrNb while retaining nearly the same radiation efficiency across the operating region, when compared to the NiZn. Figure 34, shows the radiation efficiency achieved with Sebastian's NiZn (red), CoZrNb of the same size as Sebastian (Green), and CoZrNb with volume 6 times smaller than NiZn (Blue). This shows the value hesitivity analysis brings to the engineering trade space, by decreasing the volume or increasing radiation efficiency when compared to lower hesitivity materials. Having a high hesitivity enables more trade space to shrink the total volume of the antenna or allow for increased radiation efficiency in the same size package, but it is an incomplete metric.

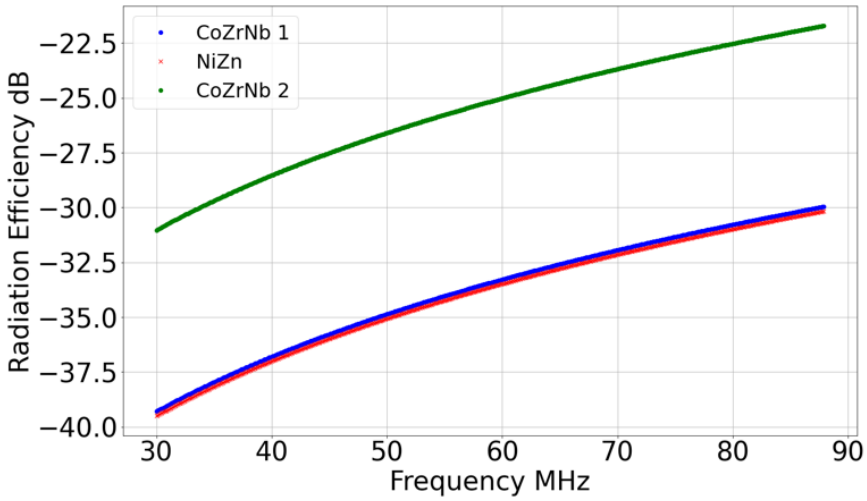

Figure 34: All three lines are the analytic radiation efficiencies of specific sized dipoles. The green line is a dipole the same size of Sebastian's NiZn (4"x1.5"x40") using CoZrNb instead of NiZn. The blue line is an approximation of how much smaller of a form factor the dipole can take using CoZrNb for the same radiation efficiency as NiZn. The small CoZrNb dipole is 2"x1"x20".

Hesitivity alone masks the trade space between initial permeability, resonant frequency, and antenna dimensions. Based on hesitivity alone, CoZrNb should be able to achieve the same radiation efficiency as NiZn in a much smaller form factor, but these two antennas are operating using different modes of radiation, which require different design considerations. In Region 3 for CoZrNb with little loss from 30-88 MHz, the TE01 mode dominates the radiation, but in order to establish a TE01 mode the permeability of CoZrNb must be taken into account. The permeability of NiZn is 4 or 5 times larger than CoZrNb in the operating frequency range and permittivity is 4 times larger as well. This places real physical constraints on the required dimensions to support the desired mode.

MEEP provides a more complete design process by utilizing 2-D cross sectional analysis as an intermediate step to computationally costly full-wave solvers. MEEP provides a computationally effective way to identify shortfalls in using the analytic efficiency equations only, creating a more complete design process.

MEEP was used to compare the same 4 inch by 1.5 inch dipoles using both NiZn and CoZrNb. MEEP was used to verify that both the NiZn dipole and the CoZrNb behave as expected. Figure 35 shows only surface wave radiation, which is expected based on Region 1 high loss operation. Figure 36 shows no radiation as expected when using CoZrNb, which operates in Region 3 which requires a supported TE01 field, and is not viable with the given dimensions. The onset for TE01 with a 4 inch by 1.5 inch dipole using CoZrNb is above the upper end of the 30-88 MHz operating frequency desired. The commercial product, while much wider and will work in the frequency range, offers very poor performance around -20dB gain [15].

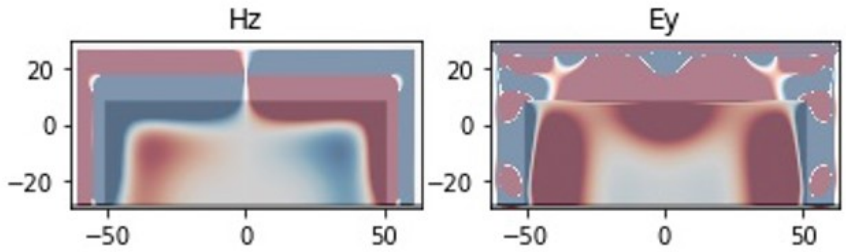

Figure 35: MEEP simulation of a 4"x1.5" NiZn dipole cross section. The radiation is surface wave only as expected. Region 1 operation in the high loss case should be surface wave radiation.

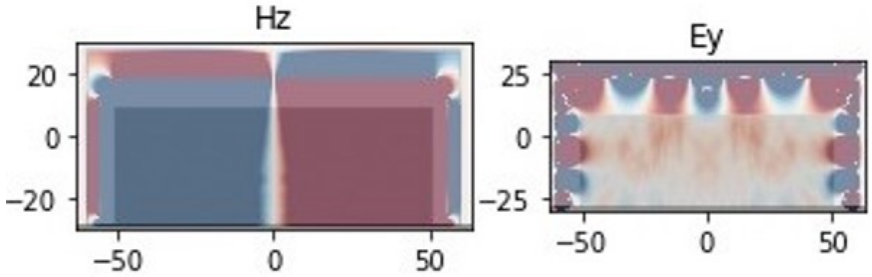

Figure 36: MEEP simulation of a 4"x1.5" CoZrNb dipole cross section. There is no supported radiation with this size cross section at the low operating frequency as expected. Region 3 operation is driven by traditional modal analysis to find a supported TE01 field.

Driving to lower frequencies requires at least a different material, if not a different

design. Yousefi began to address a different design using a truncated sunken trough design, but left it mostly unfinished.

7.2 Trough Design

The dipole and toroid configurations above a ground plane have been described and demonstrate useful results, and while they have their advantages compared to wire antennas they also possess several disadvantages as well. The first significant disadvantage is that being above a ground plane still limits how conformal the antenna can be. The second significant disadvantage is that the coaxial feed posited for these structures. Having a sensitive feed above the antenna exposes the feed to environmental concerns and is at risk of unwanted bending and strain. The commercial product encapsulates it in a dielectric capping layer to smooth and protect the feeds. The feed structure also presents modeling and simulation challenges. The trough design proposed by and partially modeled by Yousefi will be extended and examined as a solution to mitigate the disadvantages of a coax loop feed structure.

The trough design is more tractable in modeling and simulation because the coaxial feed is replaced by a wireport feed. A cross section of a wireport feed is shown in Figure 37. In 3D modeling the wireport is simply an edge broken into 3 sections and assigned an impedance. The meshing requirements for an edge versus the entire coaxial region with the dipole and toroid design is approximately 30 times less. The entire trough design including the feed only required around 25,000 mesh regions, whereas the GPS toroid required 196,000 mesh regions and Yousefi's toroid required 750,000 mesh regions. Yousefi's toroid could not be simulated with accuracy because the feed structure exhibited low frequency breakdown, as discussed in Chapter VI. The trough design allows modeling and simulation of low frequency antennas unlike the toroid and dipole antennas by removing the coax from the simulation region.

Yousefi in her dissertation outlined several significant electrical advantages the trough design offers. In addition to modeling advantages, the recessed trough is truly conformal to the ground plane and the aspect ratio of the trough impacts modal cutoffs and can be used as a tuning parameter in the design process. A slot can be added making the opening of the trough more narrow, which can be used to refine impedance matching of the antenna [5]. This offers a viable alternative to loop spacing.

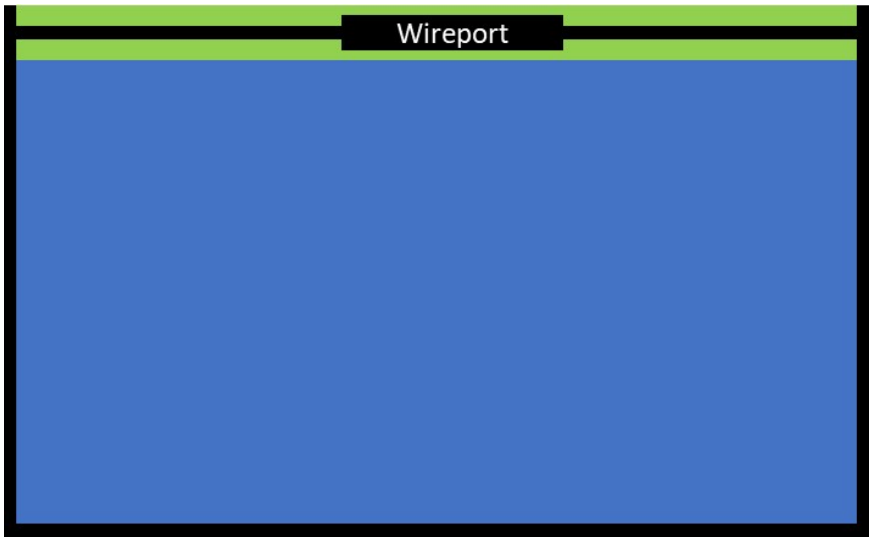

Figure 37: Cross section of a wireport feed to be used in a trough design for modeling and simulation.

Much like the dipole on a ground plane, the modes of a magneto-dielectric filled trough do not have analytic cutoff frequencies. An infinite slab on a ground plane could approximate the cutoff frequencies of the dipole and toroid configurations, but the trough more closely resembles a filled PEC-walled waveguide. Equation 37 is the closed form solution to a PEC-walled waveguide filled with magneto-dielectric infinite in the z-direction [10].

$$f_c = \frac{1}{2\pi\sqrt{\mu\epsilon}}\sqrt{\left(\frac{m\pi}{a}\right)^2 + \left(\frac{n\pi}{b}\right)^2} \tag{37}$$

To find the appropriate dimensions needed to support TE01 the height and width were varied. The same dimension ratio Yousefi used, 4.5:1, in her toroid was used to for this analysis. Figure 38 shows the required width of the trough to support TE01 within the 30-88 MHz operating region.

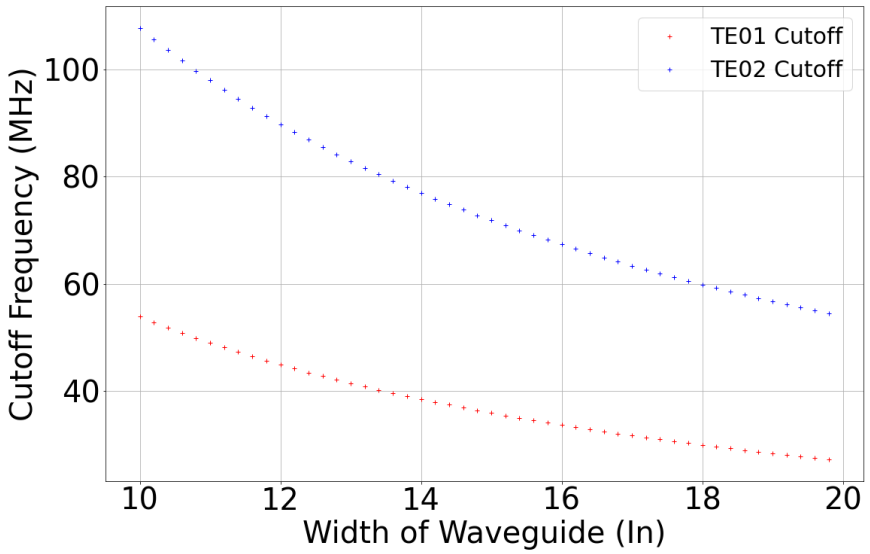

Figure 38: Analytic approximation of trough design cutoff using a rectangular waveguide filled with CoZrNb.

The width required to operate using a TE01 excitation would be around 16 inches, which is 4 times larger than the NiZn dipole. It is clear the different operating regions are important in the design process. Additionally, no dimensions can support the desired TE01 excitation over the entire 30-88 MHz desired bandwidth.

Therefore the practical lower bound of CoZrNb in the trough design will be found. A frequency of interest that this next design will include is 138-144 MHz, as well as pushing as far down from Very High Frequency (VHF) high as possible. Using Equation 37 to design the initial dimensions, MEEP was used to determine more accurate cutoff frequencies. Figure 39 shows the TE02 and TE01 cutoff frequencies based on a PEC waveguide. The solid blue horizontal lines are the frequencies of interest and the red lines are the actual cutoff frequencies found using MEEP. The green vertical

line is the size of the toroid analyzed in MEEP to get the cutoff frequencies.

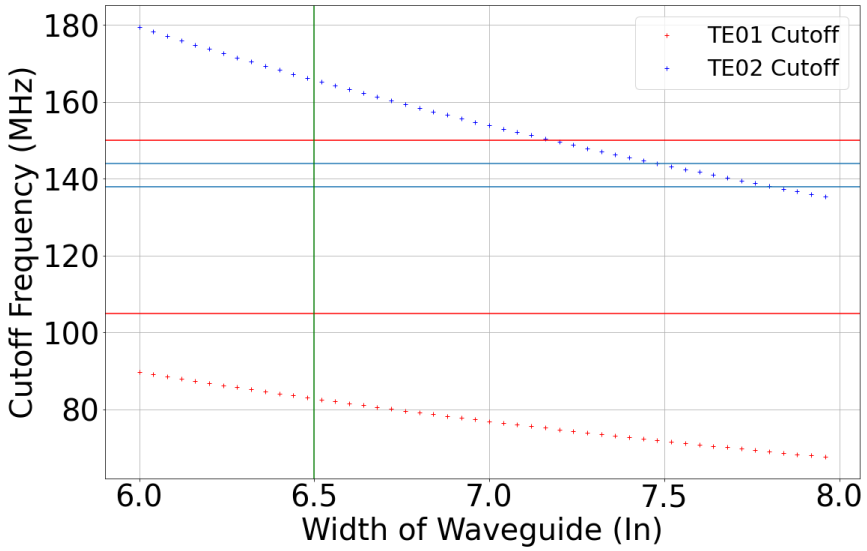

Figure 39: Analytic cutoff frequencies of a filled PEC waveguide to approximate the trough design cutoff frequencies. The horizontal red lines are the simulated MEEP trough design cutoff frequencies, which can operate from 110-150 MHz in TE01 mode.

The analytic cutoff frequencies for a filled PEC waveguide are not as well matched to the trough design as the infinite slab with the dipole above a ground plane. It does serve to narrow the FDTD simulation frequencies required to find the cutoff frequencies. With an antenna 6.5 inches wide and 1.5 inches tall CoZrNb can operate between 110 and 150 MHz based on MEEP simulations. The trough design operating in Region 3 does not receive the significant benefits of the high loss region in terms of bandwidth and begins to lose the size benefits at the lower frequencies. Even though the size of this antenna isn't as small as hesitivity suggests could be achieved, it is still extremely conformal compared to a typical 135-160 MHz antenna, at only three percent the height of a 3.9 ft commercial antenna [24]. Additionally, the trough design allows the antenna to be recessed into a vehicle body enabling flush mount designs to truly be conformal. It should be noted that this process is focused on a bar trough design, but the recessed toroid trough is applicable to all the analytic and 2D FDTD modal analysis techniques employed [5].

A truncated trough design using CoZrNb, 6.5 inches by 1.5 inches and 20 inches long was simulated in SENTRi from 100 to 200 MHz. The geometry of the trough design is shown in Figure 40. The gain is shown in Figure 41. It should be noted this uses a single feed so uniform currents may not be present along the length of the trough limiting its radiation potential.

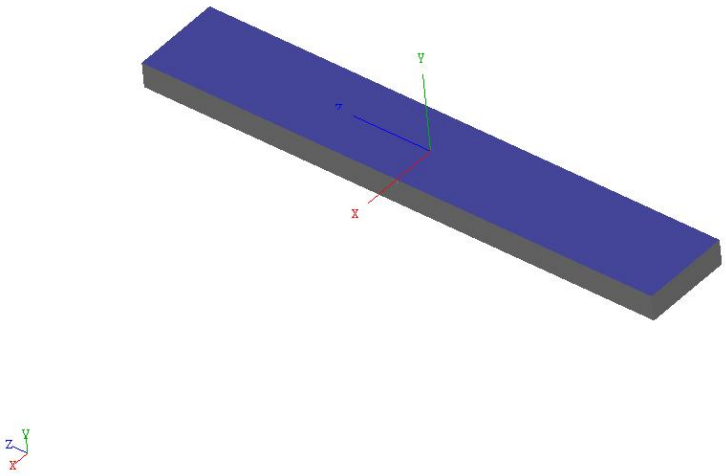

Figure 40: Trough Geometry used in full-wave simulation from 100-200 MHz.

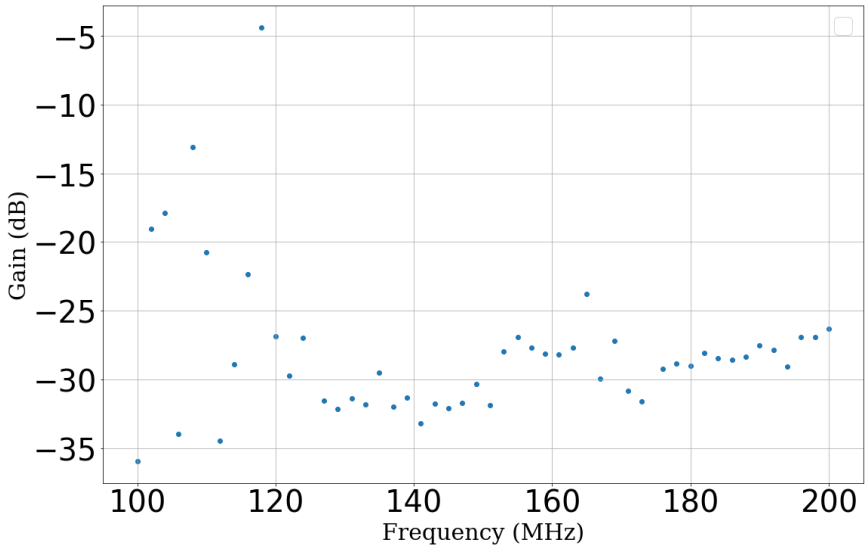

Figure 41: Modeled gain of the 6.5”x1.5” trough antenna from 100-200 MHz.

The gain is low overall, but relatively steady from 120-200 MHz. Around 110 MHz the gain is unstable, which is likely due to the 110 MHz predicted cutoff frequency for a cross section of the trough in MEEP. MEEP uses a 2D cross section of the trough that is not a complete representation of the finite length trough. The ends of the trough are capped with PEC. This leads to additional modal considerations that need to be taken into account. Equation 38 taken from Balanis [10] is the analytic cutoff frequency for a closed filled PEC cavity. The gain of the trough design could be improved by adding additional feeds throughout the length of the trough to achieve uniform internal fields and by extending the overall length. Additionally, impedance matching based on adjusting the trough slot can be completed to improve gain. Yousefi explored the trough slot improvements in her dissertation [5].

$$f_c = \frac{1}{2\pi\sqrt{\mu\epsilon}}\sqrt{\left(\frac{m\pi}{a}\right)^2 + \left(\frac{n\pi}{b}\right)^2\left(\frac{p\pi}{c}\right)^2} \tag{38}$$

A closed cavity again does not solve the modes found in the trough design, but can offer additional insight not found in the 2D FDTD simulation. The TE01 and

TE02 mode has shifted cutoffs down to 85 MHz and up to 165MHz respectively. This explains why there is no significant drop in gain below 110 MHz and also explains why there is a slight perturbation near 165 MHz. Between a closed cavity and rectangular waveguide approximation engineers can approximate the required dimensions for a given operating frequency and material. As previously discussed the trough design is readily implemented in full-wave simulations like SENTRi due to the wireport feed over the coaxial feed of the dipole and toroid. Overall the trough design offers unique design opportunities when operating in Region 3.

There are several significant design rules that should be followed with trough designs. The first significant rule is that the magneto-dielectric must be operated in Region 3 the low loss region, where $\mu' > 2\mu''$. Region 3 operation is significant because it allows the TE01 field to develop internal to the medium resulting in wavelength compression and allows a reduction in antenna size. The next significant rule focuses on the use of analytic cutoff techniques to estimate modal cutoffs of the trough design. The trough design should use both a filled PEC-walled rectangular waveguide and a filled PEC-walled cavity to estimate the cutoff frequencies. The analytic estimated cutoff frequencies should then be compared against an 2D FDTD simulation of an infinite trough design. Finally, based off the results of the analytic and 2D simulation work, a full-wave solution should be pursued. This process builds confidence in the full-wave solution and provides insight into how parameter changes can influence the full-wave simulation.

The results have made clear that CoZrNb is ill suited for lower frequencies. The commercial product struggled to achieve any meaningful performance from 30-88 MHz. The analytic cutoff approximations in this work highlight the considerable size needed to use CoZrNb at such low frequencies and was supported using 2D FDTD. The full-wave analysis of the truncated trough filled with CoZrNb highlights the

effective lower bound of CoZrNb. A new material with higher permeability is needed to achieve wavelength compression at low frequencies which still operating in Region 3.

VIII. Conclusions

The goal of this research was to extend and complete the body of work investigating the finite length dipole, toroid, and trough designs of magneto-dielectric wire antennas and magnetic flux channel antennas. Within the scope of this research my specific contributions included using analytic alternatives to estimate cutoff frequencies, using 2D Finite Difference Time-Domain (FDTD) simulations for rigorous modal analysis, using full-wave simulations to model different Magneto-Dielectric Wire Antennas (MDWA) configurations and feed structures which have previously not been addressed , highlighting several design oversimplifications the original authors used with remediation recommendations, and outlining the 3 different operating regions and design differences for MDWAs. A modified design process is therefore proposed.

It was determined that in Region 3 operation the mode of radiation is driven by a TE01 field being established in the medium. This finding was driven by traditional modal analysis as verified by Massachusets Institute of Technology Electromagnetic Equation Propagation (MEEP) 2D FDTD simulations in conjunction with closed form cutoff frequency calculations. Region 1 operates using surface wave radiation, which was determined using skin depth calculations and verified by MEEP. Region 2 is a keep out region of operation because both TE01 and surface wave radiation modes are not well established. Region 1 is the high loss case with $\mu'' > 2\mu'$. Region 3 is the low loss case with $\mu' > 2\mu''$. Region 2 lies between Regions 1 and 3. The trough design enables the use of a unique feed structure compared to the dipole and toroid configurations. The trough design can utilize a wireport feed, which enables modeling and simulation of MDWAs at much lower frequencies which will contribute to further efforts. The wireport feed mitigates the competing requirements of meshing the feed coarse enough to not experience low-frequency breakdown, but fine enough to establish a Transverse Electric and Magnetic (TEM) mode in the coax feed.

It was determined that the commercial product in the Very High Frequency (VHF) operating region performed poorly. This work investigated that poor performance and determined that CoZrNb is ill suited in the frequency range. A new material must be used to achieve good low frequency performance. The ideal permeability to work at lower frequencies must have a larger initial permeability to take advantage of the size reduction benefits, while introducing as much loss as possible while still operating in Region 3.

8.1 Future Work

The use of magneto-dielectric materials has not been fully investigated. There are several focus areas that for future work.

- Investigate thin film manufacturing techniques for filling troughs with layers of thin film in a specified orientation, or semi-rigid bars.
- Investigate the impact of adjusting thin film deposit thickness has on permeability and resonant frequency in practical layups.
- Investigate the anisotropic impact most magneto-dielectrics exhibit in the toroid, dipole, and trough configurations as it pertains to the limiting cases of dimensions driven by modal analysis.
- Investigate in depth the trough design, specifically focused on impedance matching techniques and feed design.

Bibliography

1. Thomas Sebastian. *Magneto-dielectric Wire Antennas Theory and Design*. Ph.D. Dissertation, Arizona State University, Tempe, AZ, 2013.

2. David Auckland, Rodolfo Diaz, and Karl Sieradzki. High Efficiency Radiators for Conformal Ultra-Wideband Electromagnetic Systems. Technical report, JEM Engineering, 2020.

3. D. V. Giri. Electrically small loop antenna loaded by a homogenous and isotropic ferrite cylinder-part I, 1973.

4. David Auckland. Low Profile, Very Wide Bandwidth Aircraft Communications Antennas Using Advanced Ground-Plane Techniques. Technical report, JEM Engineering, 2014.

5. Tara Yousefi. *Next Generation of Magneto-Dielectric Antennas and Optimum Flux Channels*. Ph.D. Dissertation, Arizona State Univesity, Tempe, AZ, 2017.

6. Nicole Ray and Rudy Diaz. Manufacturing and Metrology of High Magnetic Permeability Materials for High Efficiency, Wideband, and Conformal RF Antennas. Technical report, Rayn Innovations, 2014.

7. David Auckland. Synthesis and Realization of Broadband Magnetic Flux Channel Antennas. Technical report, JEM Engineering, 2016.

8. R Devore and P Bohley. The electrically small magnetically loaded multiturn loop antenna. *IEEE Trans. Antennas Propag.*, 25:496–505, 1977.

9. Tom Sebastian, Sergio Clavijo, Rodolfo Diaz, Chris Daniel, and David Auckland. A new realization of an efficient broadband conformal magnetic current dipole antenna. *IEEE Antennas Propag. Soc. AP-S Int. Symp.*, 0(1):1290–1291, 2013.

10. Constantine Balanis. *Advanced Engineering Electromagnetics*. John Wiley & Sons, Inc., second edition, 2012.

11. Soft Ferrite component, 61 Material Grade Safety Data Sheet. https://www.fair-rite.com/wp-content/uploads/2016/03/SDS-61-Component.pdf.

12. RQ-1/Mq-1 Predator Unmanned Aerial Vehicle. https://www.acc.af.mil/About-Us/Fact-Sheets/Display/Article/199130/rq-1mq-1-predator-unmanned-aerial-vehicle-retired/, 2008.

13. Bradley_Photo. Bradley Fighting Vehicle. https://www.flickr.com/photos/35703177@N00/47995737551/.

14. Edward Rothwell and Cloud Michael. *Electromagnetics*. CRC Press, third edition, 2018.

15. JEM Engineering LLC. JEM-238MFC. https://www.jemengineering.com/wp-content/uploads/2020/10/JEM-238MFC-Datasheet-Rev5.pdf.

16. RAMI Loud & Clear. AS-3900A/VRC. https://www.rami.com/product/as-3900avrc/.

17. Soft Ferrite component, 43 Material Grade Safety Data Sheet. https://www.fair-rite.com/wp-content/uploads/2016/03/SDS-43-Component.pdf.

18. Tara Yousefi, Chris B. Daniel, David T. Auckland, and Rodolfo E. Diaz. A Wideband Multimode Permeable Conformal Antenna Thinner Than $\lambda/75$ Using Advanced Ferromagnetic Laminate Composite Materials. *IEEE Antennas Wirel. Propag. Lett.*, 15:1931–1934, 2016.

19. Tara Yousefi, Student Member, and Rodolfo E Diaz. A First-Order Model of the Multiple-Feed Toroidal Magneto-Dielectric Antenna. *IEEE Trans. Antennas Propag.*, 65(11):5796–5807, 2017.

20. Constantine Balanis. *Antenna Theory*. John Wiley & Sons, Inc., third edition, 2005.

21. David Pozar. *Microwave Engineering*. John Wiley & Sons, Inc., fourth edition, 2011.

22. Karl Warnick. *Numerical Methods for Engineering An Introduction Using MATLAB and Computational Electromagetics Examples*. SciTech Publishing, 2011.

23. Pasternack. 250 Semi-rigid Coax Cable with Tinned Aluminum Outer Conductor. https://www.pasternack.com/semirigid-0.250-50-ohm-coax-cable-tinned-aluminum-pe-sr401al-p.aspx.

24. Cushcraft FM Ringo Vertical Antennas. DXEngineering. https://www.dxengineering.com/parts/csh-ar2.

Acronyms

AF Area Factor. 8

ASU Arizona State University. 3, 4, 26

DC Direct Current. 17, 19, 20

EMI Electromagnetic Interference. 15

FDTD Finite Difference Time-Domain. 2, 4, 36, 39, 50, 71, 76

FSF Field Shape Factor. 8, 9

GPS Global Positioning System. vii, 32, 33, 37, 40, 41, 42, 61, 63

HUMVEEs High Mobility Multipurpose Wheeled Vehicles. 23

MDWA Magneto-Dielectric Wire Antennas. iv, 1, 2, 3, 11, 24, 25, 26, 27, 29, 30, 31, 57, 76, 1

MEEP Massachusets Institute of Technology Electromagnetic Equation Propagation. vii, 39, 50, 54, 63, 70, 71, 76

MFC Magnetic Flux Channels. iv, 1, 2, 4, 20, 21, 22, 24, 32, 58, 1

PEC Perfect Electric Conductor. viii, 59, 69, 70, 71, 73

PMC Perfect Magnetic Conductor. 11, 25, 54

RF Radio Frequency. 3

SENTRi Scalable Engineering Tools for RF Integration. 41

SIBR Small Business Innovation Research. 4

TE01 Transverse Electric. 28, 29, 30, 35, 36, 37, 39, 41, 48, 51, 52, 53, 54, 63, 66, 70

TEM Transverse Electric and Magnetic. 59, 76

VHF Very High Frequency. 26, 70, 77

VSWR Voltage Standing Wave Ratio. 45, 46, 47, 48

REPORT DOCUMENTATION PAGE

Form Approved
OMB No. 0704–0188

1. REPORT DATE *(DD–MM–YYYY)*	2. REPORT TYPE	3. DATES COVERED *(From — To)*
24–03–2022	Master's Thesis	September 2020 — March 2022

4. TITLE AND SUBTITLE

Magnetic Flux Channel Antenna Design
In Conformal Applications

5a. CONTRACT NUMBER

5b. GRANT NUMBER

5c. PROGRAM ELEMENT NUMBER

6. AUTHOR(S)

Tremblay, William J, Capt, USAF

5d. PROJECT NUMBER

5e. TASK NUMBER

5f. WORK UNIT NUMBER

7. PERFORMING ORGANIZATION NAME(S) AND ADDRESS(ES)

Air Force Institute of Technology
Graduate School of Engineering and Management (AFIT/EN)
2950 Hobson Way
WPAFB OH 45433-7765

8. PERFORMING ORGANIZATION REPORT NUMBER

AFIT-ENG-MS-22-M-069

9. SPONSORING / MONITORING AGENCY NAME(S) AND ADDRESS(ES)

Intentionally Left Blank

10. SPONSOR/MONITOR'S ACRONYM(S)

11. SPONSOR/MONITOR'S REPORT NUMBER(S)

12. DISTRIBUTION / AVAILABILITY STATEMENT

DISTRIBUTION STATEMENT A:
APPROVED FOR PUBLIC RELEASE; DISTRIBUTION UNLIMITED.

13. SUPPLEMENTARY NOTES

14. ABSTRACT

MFC and MDWA are effective, and in some cases, superior alternatives to traditional metallic antennas, particularly in conformal and electrically small applications at the cost of fabrication and feed complexity. The frequency dispersive nature of magnetic material constituent parameters imposes operating frequency constraints on the antenna design process, which were not fully developed in prior art. This research quantifies the key differences between the operating regions of magneto-dielectric materials for antenna applications and demonstrates the effectiveness of numerical method augmented modal analysis in the design process, regardless of operating region. Modeling challenges associated with MDWAs are addressed leading to novel full wave modeling results for antennas designed in accordance with early MDWA design law. The results clarify the limitations of certain prior art in the recommended design process, and provide needed support for later-art material selection and design recommendations.

15. SUBJECT TERMS

MFC-Magnetic Flux Channel, MDWA-Magneto-Dielectric Wire Antennas

16. SECURITY CLASSIFICATION OF:			17. LIMITATION OF ABSTRACT	18. NUMBER OF PAGES	19a. NAME OF RESPONSIBLE PERSON
a. REPORT	b. ABSTRACT	c. THIS PAGE			Lt Col Michael D. Seal, AFIT/ENG
U	U	U	UU	93	19b. TELEPHONE NUMBER *(include area code)* (937) 255-3636 x3305; michael.seal@afit.edu

Standard Form 298 (Rev. 8–98)
Prescribed by ANSI Std. Z39.18